The Astrophysical Journal, 658:1027–1046, 2007 April 1
© 2007. The American Astronomical Society. All rights reserved. Printed in U.S.A.

THE *SPITZER* SURVEY OF THE SMALL MAGELLANIC CLOUD: FAR-INFRARED EMISSION AND COLD GAS IN THE SMALL MAGELLANIC CLOUD

Adam Leroy,[1,2] Alberto Bolatto,[2] Snezana Stanimirovic,[2,3] Norikazu Mizuno,[4] Frank Israel,[5] and Caroline Bot[6]
Received 2006 August 21; accepted 2006 November 15

ABSTRACT

We present new FIR maps of the SMC at 24, 70, and 160 μm obtained as part of the *Spitzer* Survey of the Small Magellanic Cloud (S^{3}MC). These maps cover most of the star formation in the SMC bar and wing. We combine our maps with literature data to derive the dust mass surface density across the SMC. We find a total dust mass of $M_{\rm dust} = 3 \times 10^5\ M_\odot$, implying a dust-to-hydrogen ratio over the region studied of $\log_{10}({\rm D/H}) = -2.86$, or 1:700, which includes H_2. Assuming the dust to trace the total gas column, we derive H_2 surface densities across the SMC. We find a total H_2 mass $M_{H_2} = 3.2 \times 10^7\ M_\odot$ in a distribution similar to that of the CO, but more extended. We compare profiles of CO and H_2 around six molecular peaks; on average H_2 is more extended than CO by a factor of $\sim$1.3. The implied CO-to-H_2 conversion factor over the whole SMC is $X_{\rm CO} = (13 \pm 1) \times 10^{21}$ cm^{-2} (K km s^{-1})$^{-1}$. Over the volume occupied by CO the conversion factor is lower, $X_{\rm CO} = (6 \pm 1) \times 10^{21}$ cm^{-2} (K km s^{-1})$^{-1}$, but still a few times larger than that found using virial mass methods. The molecular peaks have H_2 surface densities $\Sigma_{H_2} \approx 180 \pm 30\ M_\odot$ pc^{-2}, similar to those in Milky Way GMCs, and correspondingly low extinctions, $A_V \sim 1$–2 mag. The theory of photoionization-regulated star formation predicts $A_V \sim 6$, which would require the GMCs to be $\sim$3 times smaller than our 46 pc resolution element. For a given hydrostatic gas pressure, the SMC has a 2–3 times lower ratio of molecular to atomic gas than spiral galaxies. Combined with lower mean densities, this results in this galaxy having only 10% of its gas in the molecular phase.

Subject headings: dust, extinction — galaxies: ISM — infrared: ISM — ISM: molecules — Magellanic Clouds

1. INTRODUCTION

Dust grains play a central role in the formation of stars from atomic gas. Dust shields molecular gas from dissociating radiation and allows it to cool and condense to the densities necessary to form stars. The surfaces of dust grains serve as the sites of molecular hydrogen formation. In low-metallicity galaxies, an underabundance of dust may result in more intense radiation fields, different thermal balance in the interstellar medium (ISM), and different structure for giant molecular clouds (GMCs). However, there are only a few low-metallicity systems in which atomic gas, molecular gas, dust, and star formation tracers have all been mapped at resolution sufficient to resolve individual star-forming regions or GMCs ($\lesssim$100 pc).

In this paper we present new far-infrared (FIR) images of the Small Magellanic Cloud (SMC) obtained using the *Spitzer Space Telescope* as part of the *Spitzer* Survey of the Small Magellanic Cloud (S^{3}MC; Bolatto et al. 2007). We combine these maps with previous FIR, H I, and CO data to construct a complete picture of the star-forming ISM in this nearby low-metallicity galaxy. We focus on three questions: (1) What is the mass of dust in the SMC? (2) How much molecular hydrogen (H_2) is in the SMC? (3) How does the distribution of H_2 in the SMC, particularly its structure and relation to CO emission, compare to that in the Milky Way? In this introduction we describe the SMC and expand on these questions.

The SMC is the nearest actively star-forming, low-metallicity ($Z \lesssim 1/10\ Z_\odot$) galaxy. It is therefore a good location to study the relationship between gas, dust, and star formation at low metallicity. It forms stars at $\sim$0.05 $M_\odot$ yr^{-1} (Wilke et al. 2004), a normalized rate that is comparable to that of the Milky Way (the dynamical mass of the SMC is $\sim 2 \times 10^9\ M_\odot$; Stanimirović et al. 2004). It is gas-rich, with $\approx 4 \times 10^8\ M_\odot$ of atomic gas in an extended distribution (Stanimirović et al. 1999) and a comparable mass of stars, $\sim 3 \times 10^8\ M_\odot$ (estimated from the DIRBE 2.2 μm data). The SMC is also unenriched in heavy elements, with an oxygen abundance just above 1/10 solar [$12 + \log({\rm O/H}) = 8.0$; Dufour 1984]. At a distance of 61.1 kpc (Hilditch et al. 2005; Keller & Wood 2006), even modest telescopes can observe the SMC with excellent spatial resolution, and at a Galactic latitude of $b = -44^\circ$ it is obscured by little foreground material.

Several recent studies have used FIR emission to study the dust in the SMC, finding evidence for a low dust-to-gas ratio (DGR). Stanimirović et al. (2000) modeled HIRAS data (a high-resolution *IRAS* product) and found that the SMC had an unexpectedly low dust mass of only $1.8 \times 10^4\ M_\odot$. The corresponding DGR is 2 orders of magnitude below the Galactic value. Bot et al. (2004) studied the diffuse gas using the *Infrared Space Observatory* (*ISO*) and *IRAS* data and found that the emissivity of diffuse SMC gas is 30 times lower than that of high-latitude Galactic gas. Wilke et al. (2004) studied emission integrated over the whole SMC, also using *ISO* data. They fitted the dust using several blackbodies and found a much higher total dust content than previous studies, $7.8 \times 10^5\ M_\odot$. Using this result, they derived a DGR only a few times lower than the Galactic value.

Only $1.7 \times 10^5\ M_\odot$ of the dust mass obtained by Wilke et al. (2004) would be estimated from their FIR data alone. The rest is in a cold component that emits at millimeter wavelengths, with a temperature of $\sim$10 K. Stanimirović et al. (2000) also recognized the possibility of a large mass of cold dust from the 140 and 240 μm DIRBE data, which show higher intensities than those allowed by a single population of Galactic dust that fits the *IRAS* measurements. Aguirre et al. (2003) demonstrated that this excess extends out to 1.2 mm by measuring the spectrum of the

[1] Max-Planck-Institut für Astronomie, Heidelberg, Germany.
[2] Radio Astronomy Laboratory, University of California, Berkeley, CA.
[3] Department of Astronomy, University of Wisconsin, Madison, WI.
[4] Department of Astrophysics, Nagoya University, Nagoya, Japan.
[5] Sterrewacht Leiden, Leiden, Netherlands.
[6] *Spitzer* Science Center, California Institute of Technology, Pasadena, CA.

SMC using the TopHat balloon. They also showed, however, that the measurements can be fitted by a single dust population if $\beta = 1$ for the dust emissivity law, $\tau \propto \lambda^{-\beta}$.

In addition to providing information about the dust, the FIR emission can be used to trace molecular gas. Clouds of molecular hydrogen are the sites of star formation, but H_2 cannot be observed directly under the conditions found in GMCs because it lacks a permanent dipole moment and T is too low to excite the quadrupole transitions. Observations of tracer molecules, particularly CO, often substitute for direct observations of H_2. In low-metallicity galaxies, the lack of heavy elements and the lower DGR may alter the structure of molecular clouds and affect the relationship between tracer molecules and H_2, leaving the amount of molecular gas in these systems uncertain. Unlike the CO-to-H_2 ratio, the dust-to-hydrogen ratio, D/H, can be measured away from molecular clouds using H I and FIR emission. Under the assumption that D/H varies slowly, FIR emission may provide a better estimate of the amount of H_2 in these systems than CO observations.

The molecular hydrogen content of the SMC may be even less well known than its dust content. Mizuno et al. (2001) and N. Mizuno et al. (2007, in preparation) surveyed the CO $J = 1 \rightarrow 0$ line across most of the SMC using the NANTEN telescope and found a luminosity of $\sim 1 \times 10^5$ K km s^{-1} pc^2. They used the virial mass method to derive a CO-to-H_2 conversion factor, $X_{\rm CO}$, of $(1\text{–}5) \times 10^{21}$ cm^{-2} (K km s^{-1})$^{-1}$, about 10 times the Galactic value [$X_{\rm CO}^{\rm Gal} \approx 2 \times 10^{20}$ cm^{-2} (K km s^{-1})$^{-1}$]. This implies a total molecular mass of $M_{\rm mol} \sim (2\text{–}10) \times 10^6\ M_\odot$. Blitz et al. (2007) corrected these data for resolution and sensitivity effects and found a value of $X_{\rm CO}$ toward the low end of this range, $(1\text{–}1.5) \times 10^{21}$ cm^{-2} (K km s^{-1})$^{-1}$, implying $M_{\rm mol} \sim (2\text{–}3) \times 10^6\ M_\odot$. Considering individual regions with better spatial resolution, Rubio et al. (1993) and Bolatto et al. (2003) both found conversion factors a few times the Galactic value, although dependent on the size of the structure studied.

Modeling of the FIR can be used to derive the mass and structure of H_2 without relying on the assumptions that CO and H_2 have the same structure and that GMCs are in virial equilibrium. If the gas and dust are well mixed and properties do not vary too dramatically between the molecular and atomic ISM, the dust acts as an optically thin tracer of the total, H I + H_2, gas surface density. Dame et al. (2001) demonstrated this method to work by comparing *IRAS* to CO and H I emission in the Milky Way (see also Reach et al. 1998). Israel (1997b) used *IRAS* to study the SMC and found a total H_2 content of $7.5 \times 10^7\ M_\odot$ and the CO-to-H_2 conversion factor to be 60 times the Galactic value. In this paper we use a similar method to construct H_2 maps with 46 pc resolution and sensitivity to H_2 surface densities as low as $\sim 20\ M_\odot$ pc^{-2} (3 σ).

Using the H_2 map, we test three predictions regarding molecular gas in low-metallicity systems. McKee (1989) argued that photoionization by far-ultraviolet photons sets the level of ionization inside GMCs and thus regulates their structure. Magnetic fields couple to the ionized gas and support cores against collapse. Thus, the level of ionization is tied to the rate of star formation in the cloud. Low-mass star formation provides feedback that keeps the mean extinction, and with it the ionization level, across the cloud at a particular value. In the Milky Way this value is $\bar{A}_V \sim 4\text{–}8$, independent of cloud mass. In low-metallicity systems, with low DGRs, McKee (1989) predicts that GMCs will require higher gas surface densities, $\Sigma_{\rm H\,I+H_2}$, in order to achieve the same mean extinctions found in the Milky Way. For the low DGR in the SMC, this implies GMCs with $\Sigma_{\rm H\,I+H_2} \gtrsim 1000\ M_\odot$ pc^{-2} (see also Pak et al. 1998). Second, CO in the SMC may be underabundant or absent in regions where H_2 survives because the H_2 self-shields, but this does not stop photodissociation of the CO (e.g., Maloney & Black 1988). Third, Blitz & Rosolowsky (2004) showed that there is a good correlation between the midplane hydrostatic pressure and the ratio of molecular to atomic gas along lines of sight toward spiral galaxies. We test whether this correlation extends to the low-metallicity, low-pressure environment found in the SMC, or whether metallicity acts as a "third parameter" in the relationship between pressure and molecular gas fraction.

This paper is organized as follows: In § 2 we discuss the new *Spitzer* maps and the literature data we use to supplement them. We describe our foreground subtraction and discuss uncertainties in the data. In § 3 we present the new maps and literature data on a common astrometric grid. We construct maps of dust and H_2 and present an updated FIR spectral energy distribution (SED). In § 4 we consider the relationship between dust and gas, including the DGR, the CO-to-H_2 conversion factor, the structure of molecular clouds, and pressure and extinction in the star-forming regions. In § 5 we present our conclusions.

2. DATA

To meet the science goals described in the introduction, we require FIR images of the SMC at several wavelengths on a common astrometric grid with good relative calibration. These allow us to derive maps of the dust and H_2 content in § 3 and add new points at 24, 70, and 160 μm to the integrated SED of the SMC. We start with the new *Spitzer* images of the SMC from S^{3}MC at 24, 70, and 160 μm and supplement these data with images at 60 and 100 μm from *IRAS* and at 170 μm from *ISO*. We use data from DIRBE from 25 to 240 μm as the basis for the flux calibration and consider TopHat data (Aguirre et al. 2003) when constructing the integrated SED. The wavelengths, telescopes, limiting resolution, and references for the data used in this paper are listed in Table 1. In the rest of this section we describe how we isolate the emission from the SMC in the FIR images and estimate the uncertainties in the final maps.

2.1. *Color Corrections and Flux Definitions*

Throughout this paper we quote monochromatic flux densities assuming an $F_\nu \propto \nu^{-1}$ SED across the relevant bandpass. This is the convention for *IRAS*, IRAC, and DIRBE but differs from the MIPS standard, which is to assume a Rayleigh-Jeans tail ($F_\nu \propto \nu^2$) across the bandpass. We apply color corrections to the MIPS data at 24, 70, and 160 μm by dividing by 0.961, 0.918, and 0.959, respectively, before any processing to bring them to the *IRAS* definition. For most of the work in this paper, this choice is arbitrary.

2.1.1. *Bright Pixel Removal*

Before other processing we remove pixels with unexpectedly high intensities from the 24, 70, and 160 μm maps (>100, >200, and >250 MJy sr^{-1}, respectively). At 24 μm these pixels correspond to point sources and are well over the saturation limit, at 160 μm these are simply artifacts, and at 70 μm they are a mix of the two. Removing these point sources lowers the integrated flux in the foreground-subtracted 24 μm map by $\approx$15%. The effect on the flux at 70 μm is negligible ($\sim$1%). We interpolate to fill these pixels using nearby data when placing the maps at a common resolution by taking the beam-weighted mean of all nearby unflagged data.

TABLE 1
Data Sets Used in This Paper

Nominal Wavelength (μm)	Data Set	Limiting Resolution	Spatial Resolution[a] (pc)	References
24, 70, 160	MIPS (*Spitzer*)	40″	12	Bolatto et al. (2007)
25, 60, 100, 140, 240[b]	DIRBE (*COBE*)	0.7°	750	Hauser et al. (1998)
25, 60, 100	HIRAS (*IRAS*)	1.7′	30	Stanimirović et al. (2000)
25, 60, 100	IRIS (*IRAS*)	4.3′	76	Miville-Deschênes & Lagache (2005)
170	ISOPHOT (*ISO*)	1.5′	27	Bot et al. (2004)
H I	ATCA + Parkes	1.5′	27	Stanimirović et al. (1999)
CO	NANTEN	2.6′	46	Mizuno et al. (2001); N. Mizuno et al. (2007, in preparation)

[a] At our adopted distance of 61.1 kpc (Hilditch et al. 2005; Keller & Wood 2006).
[b] The DIRBE ZSMA data are the basis of our photometric calibration in this paper.

2.2. *Foreground Removal*

The intensity in the FIR maps is the sum of emission from the source and several foregrounds,

$$I_{\rm FIR} = I_{\rm zod} + I_{\rm Gal+CIB} + I_{\rm source}. \quad (1)$$

$I_{\rm zod}$ is the intensity of zodiacal light, which dominates the foreground at shorter wavelengths (12–70 μm). $I_{\rm Gal+CIB}$ is Galactic dust emission and a small diffuse cosmic infrared background (CIB) term. This is the primary foreground at longer wavelengths (100–240 μm).

2.2.1. *Zodiacal Light*

The HIRAS, IRIS, *ISO*, and DIRBE data have all been corrected for zodiacal light. We estimate the contribution of zodiacal light to the MIPS maps using the model of interplanetary dust by Kelsall et al. (1998) implemented in the *Spitzer* Observation Planning Tool. A planar fit derived to this model near the SMC for our observations is

$$I_{\rm zod} = I_{0,\,\rm zod}[0.006(l - l_{\rm SMC}) - 0.003(b - b_{\rm SMC}) + 1], \quad (2)$$

where $I_{0,\,\rm zod}$ is the intensity of zodiacal light at the nominal center of the SMC ($l = 302.7969^\circ$, $b = -44.2992^\circ$) on the date of the observations. At 24, 70, and 160 μm, respectively, $I_{0,\,\rm zod}$ is 20.1, 5.3, and 0.9 MJy sr^{-1} (98%, 36%, and 6% of the total flux, respectively). The variation in $I_{\rm zod}$ over the several days during which the observations were taken is minimal.

2.2.2. *Galactic Foreground and Cosmic Infrared Background*

At 100 μm and longer wavelengths the Galactic ISM contributes the largest foreground. We apply a similar treatment to Bot et al. (2004) and estimate the Galactic foreground along lines of sight toward the SMC using the Galactic H I column density, which is clearly separated from the SMC H I column density by its velocity. We use the Galactic H I column density observed at $\sim 0.5^\circ$ resolution from the southern survey by Bajaja et al. (2005). For the IRIS 100 μm map, we use the fit of FIR intensity to H I column density by Boulanger et al. (1996). At 160 and 170 μm, we interpolate from the fits at 140 and 240 μm by Boulanger et al. (1996) into these bands using their best-fit temperature $T = 17.5$ K and emissivity $\beta = 2$. The median intensity of the Galactic foreground plus CIB is 1.8, 4.7, and 4.8 MJy sr^{-1} at 100, 160, and 170 μm, respectively.

For the 60 and 70 μm maps, the foreground due to Galactic dust is small, but Boulanger et al. (1996) do not provide fits for these bands. We use estimates of the emission of local dust per unit H I column density at 60 μm from Désert et al. (1990) and interpolate to 70 μm using the average colors in the map. This calculation is approximate, but the median intensity of this foreground at these wavelengths is small: 0.5 and 1 MJy sr^{-1}, or $\lesssim$20% of the zodiacal light foreground.

We do not subtract any foregrounds from the HIRAS maps; Stanimirović et al. (2000) define regions of sky near the SMC as blank and subtract a single foreground that includes zodiacal light, the Galactic foreground, and the CIB. Because we do not have an independent estimate of the zodiacal light for these data, we cannot break this foreground into its individual components. Instead, we bring the HIRAS data onto a consistent foreground subtraction by comparing them to the foreground-subtracted IRIS data at a common resolution. We find that offsets of 0.75 and 1.5 MJy sr^{-1} at 60 and 100 μm, respectively, are needed to bring the HIRAS zero level into agreement with IRIS. After this correction, the agreement between the two *IRAS* data sets is excellent.

2.2.3. *Foreground Subtracting the DIRBE Data*

The DIRBE zodiacal-subtracted mission average (ZSMA) maps appear to have a small amount of residual zodiacal light, $\sim$1 MJy sr^{-1} judging from a plot of intensity as a function of H I column over the whole sky. Therefore, we treat the DIRBE foreground subtraction separately. We derive DIRBE intensities as a function of H I column density near the SMC (within 10° of the optical center) but offset enough that we see only Galactic FIR emission (more than 3° away from the optical center). Then, for lines of sight toward the SMC we measure the Milky Way H I column density as above and subtract the average intensity of lines of sight with the same H I column density away from the SMC. This is our estimate of the DIRBE foreground, which should account for Galactic emission, the CIB, and residual zodiacal light.

The DIRBE 25 μm data are overwhelmingly contaminated by zodiacal light. We fit a plane to the nearby data and subtract this foreground before using it.

2.2.4. *The MIPS* 24 μm *Map Foreground*

In the case of the 24 μm map there are large regions of the map free of diffuse emission. Because the zodiacal light foreground is large and potentially uncertain at 24 μm and we do not have an estimate of the Galactic foreground, we use blank regions in the *Spitzer* map to estimate the residual foreground. We measure an additional foreground with a median value of 2.5 MJy sr^{-1} above and beyond the original zodiacal light foreground (§ 2.2.1). This

TABLE 2
Random Uncertainties in FIR Maps

Data Set	σ (MJy sr^{-1})	
	Native Resolution[a]	IRIS Resolution[b]
24 μm[a] MIPS (*Spitzer*).....	0.02	0.01
60 μm HIRAS (*IRAS*).....	0.07	0.02
60 μm IRIS (*IRAS*).....	0.02	0.02
70 μm[a] MIPS (*Spitzer*).....	0.34	0.06
100 μm HIRAS (*IRAS*).....	0.10	0.05
100 μm IRIS (*IRAS*).....	0.05	0.05
160 μm MIPS (*Spitzer*).....	0.58	0.10
170 μm ISOPHOT (*ISO*).....	0.22	0.05

[a] 24 and 70 μm data convolved to 160 μm resolution.
[b] Uncertainty after convolution to the IRIS (4′) resolution.

value is probably too large to be due to the Galactic foreground alone and may represent a failure in the zodiacal light model or a calibration error for MIPS. The presence of blank sky in the 24 μm map makes it easy to remove, regardless.

2.2.5. *Consistency and Calibration*

We check the calibration of the high-resolution data against DIRBE and find generally good agreement. The fluxes from each map integrated over the whole SMC agree (see Table 3 below). The exception is the MIPS 160 μm map, which contains substantially more flux than we estimate based on the DIRBE data. A central goal of the DIRBE mission was to obtain absolute brightness maps of the sky (Hauser et al. 1998), and those data represent a more reliable measurement of the flux than our MIPS map. Therefore, we calibrate the 160 μm to match DIRBE by rescaling the map. Appendix A describes how we carry out this calibration in detail. The MIPS 70 μm map is consistent with the data at 60 and 100 μm, but because the SED has a very steep slope over the MIPS 70 μm bandpass, this consistency is not a particularly strong constraint. It is not possible to perform the same sort of detailed calibration we adopt at 160 μm for the 70 μm map.

2.2.6. *Saturation*

Saturation may represent a concern over part of our 160 μm map. The bright star-forming region in the southwest of the galaxy contains a significant region with brightness greater than 50 MJy sr^{-1}, the nominal saturation limit for our medium-speed scan maps. A few other star-forming regions (N76 to the north and N83 in the east) also contain small regions with intensities above 50 MJy sr^{-1}. In total, 13% of the flux and 2.5% of the area are in regions with intensities above the saturation limit. In these regions, the response of detector becomes nonlinear and we have an additional gain uncertainty. The figure in Appendix A shows that in the southwest of the bar (the source of the lines of sight with intensities $\geq$25 MJy sr^{-1} at the DIRBE resolution) the MIPS data are $\sim$20%–30% lower than the DIRBE data. Outside this region, the MIPS and DIRBE data are well matched after correction.

2.3. *Uncertainties in the Final Maps*

We estimate the statistical uncertainties for the FIR data from the scatter about the median in regions of low intensity emission. We fit a Gaussian to the residuals about the local median taken over at $4' \times 4'$ region, so that for each point $I_{\rm resid} = I_{\rm map} - I_{\rm median}(\pm 2')$, with $I_{\rm median}(\pm 2')$ the median over a $4' \times 4'$ box centered on that point. We conduct these measurements in regions of low intensity emission outside the main body of the galaxy

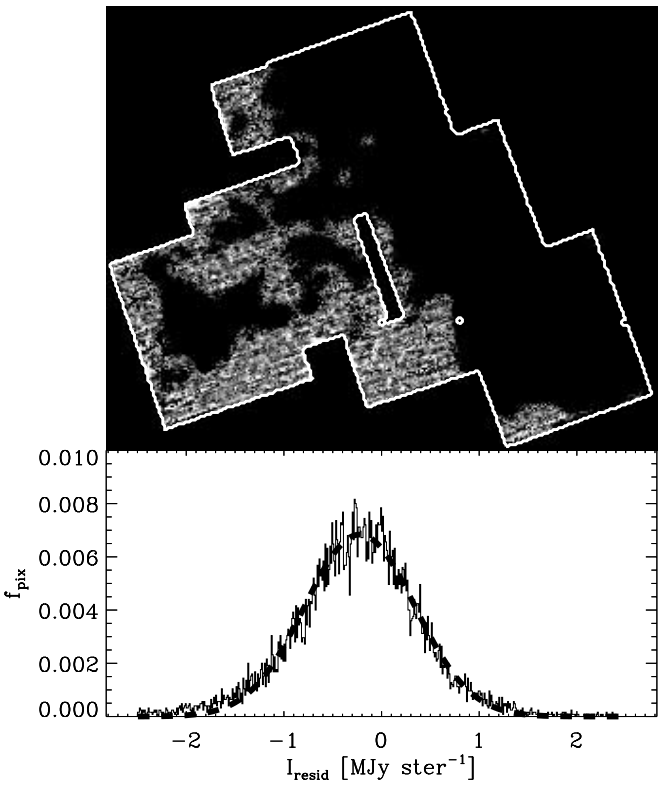

Fig. 1.—*Top*: Map used to measure the noise at 160 μm. The map shows fluctuations of the 160 μm MIPS map about the local median (over a $4' \times 4'$ box centered on the pixel). Regions with bright emission or no data are blanked out and appear black. Artifacts, particularly striping along the direction of the map, contribute to the noise, but very little extended structure is visible. The extent of the MIPS 160 μm map is shown by the white border. *Bottom*: Histogram of the residuals about the median. The dashed lines shows the best-fit Gaussian, which has $\sigma_{160} = 0.58$ MJy sr^{-1}.

to minimize the effect of structure on the measurement. However, emission with small-scale structure and artifacts present in the MIPS and *ISO* maps contribute to the noise values. These are legitimate sources of uncertainty because they affect measurements.

Table 2 gives the results of our noise estimates, and Figure 1 shows a map and histogram of deviations about the median for the MIPS 160 μm data. Two artifacts of small-scale structure are visible: the tail of low, but nonzero, values toward negative intensities and the slight shift of the center of the Gaussian toward negative intensities. Table 2 gives the noise for each map at the native and IRIS resolution. For most maps, the noise scales approximately as expected with averaging. Deviations from this scaling may be the result of artifacts such as the visible striping at low intensity in the MIPS data.

Because we calibrate our data against DIRBE, the absolute uncertainties in DIRBE are relevant to our data. Hauser et al. (1998) give the absolute gain uncertainty for DIRBE at 25, 60, 100, 140, and 240 μm as 15.1%, 10.4%, 13.5%, 10.6%, and 11.6%, respectively. The uncertainties in the absolute offset of the DIRBE data are all small enough to be negligible for our purposes. As a result of gain uncertainties for DIRBE, the minimum systematic uncertainty in any absolute flux or intensity in this paper is $\sim$10%.

The systematic uncertainty associated with the foreground subtraction is ± 1 MJy sr^{-1}. This is the approximate magnitude of the scatter about our best fits of DIRBE intensity to H I column density ($\sim$0.2 MJy sr^{-1} at 100 μm, $\sim$1.2 MJy sr^{-1} at 240 μm); it

is also about the magnitude of the offset needed to bring IRIS and HIRAS into rough agreement ($\sim$0.75 and 1.5 MJy sr^{-1}).

3. RESULTS

In this section we present maps of FIR emission and neutral gas from the SMC. We use these maps to derive the dust and molecular gas surface density, and we present an updated SED of the SMC that includes the new 24, 70, and 160 μm data.

3.1. *FIR Maps of the SMC*

Figure 2 shows the relative extent of 160 μm (*red*), 24 μm (*green*), and 8 μm (*blue*) emission in the S^{3}MC maps (Bolatto et al. 2007). The 160 μm emission is bright over the whole SMC bar in the west and in the N83/N84 star-forming region far to the east. This emission comes mostly from big grains (BGs; $a \approx$ 15–110 nm) with $T \sim 20$ K with a small (few percent) contribution from the [C II] 158 μm line (see Appendix A). Every region in the S^{3}MC map shows some 160 μm emission, including the SMC wing, which is roughly perpendicular to and east of the bar and contains more diffuse gas. By contrast, the 24 μm emission and the 8 μm emission are both confined to regions of active star formation and point sources. Much of the 24 μm emission comes from stochastically heated very small grains (VSGs), although very hot ($\sim$100 K) large grains may also make a contribution. In environments similar to the solar neighborhood, most strong 8 μm emission appears to originate from polycyclic aromatic hydrocarbons (PAHs). However, VSGs may produce emission in this band even if PAHs are absent. All three bands are brightest toward the N66 star-forming region in the southwest part of the galaxy. This is the brightest star-forming region in the SMC, home to $\sim$60 O stars (Massey et al. 1989).

Figures 3 and 4 show FIR emission and neutral gas in the SMC. Figure 3 shows the MIPS and IRIS images after foreground subtraction and processing. Figure 4 shows H I column density for the SMC from Stanimirović et al. (1999) and the CO intensity map from the NANTEN survey by Mizuno et al. (2001) and N. Mizuno et al. (2007, in preparation). The CO map is masked using a threshold contour of 0.3 K km s^{-1} (3 σ), which is then expanded by 1′ in all directions.

3.2. *Dust Content of the SMC*

Figure 5 shows dust surface density across the SMC. We describe how we construct the map in Appendix B. Briefly, we use the models by Dale & Helou (2002) to derive the dust mass surface density across the SMC. These models assume the dust along each line of sight to be heated by a power-law distribution of radiation fields; we estimate the power-law index from the 100 μm–to–160 μm color. Appendix B also gives the uncertainties associated with the dust map: a small $\lesssim$10% statistical error, an additional 20% systematic uncertainty from our foreground subtraction, and a factor of 2–3 systematic uncertainty associated with the choice of emissivity and model are the most important. Over the region covered by the MIPS 160 μm map, we find a total dust mass of $M_{\rm dust} = 3 \times 10^5\ M_\odot$.

The SMC must have $M_{\rm dust} \gtrsim 10^4\ M_\odot$ of dust; this value comes from assuming that a single population of grains is responsible for the emission in the *IRAS* 60 and 100 μm bands. This is approximately the value obtained by Stanimirović et al. (2000) and Schwering (1988). In this case, the emissivity will need to have a wavelength dependence of $\beta \sim 1$ in order to match the emission observed at 140 μm and beyond.

Several estimates lead to an upper limit to the dust mass of $M_{\rm dust} \lesssim 10^6\ M_\odot$. A Galactic DGR, DGR$_{\rm MW} \sim 10^{-2}$, applied to the mass of H I in the SMC yields $M_{\rm dust} \lesssim 4 \times 10^8\ M_\odot \times 10^{-2} \approx 4 \times 10^6$. It is well established that the DGR in the SMC is lower than the Galactic one, so this represents a firm upper limit. The heavy-element abundance in the SMC is $\approx$0.15 that of the Galaxy (measured from H II regions; Dufour 1984), and the total H I content of the SMC is $4 \times 10^8\ M_\odot$ (Stanimirović et al. 1999), so the total mass of heavy elements in the ISM of the SMC is $\sim 1.2 \times 10^6\ M_\odot$. Because the mass of dust cannot exceed the mass of heavy elements, this represents another, similar, upper limit to the dust content.

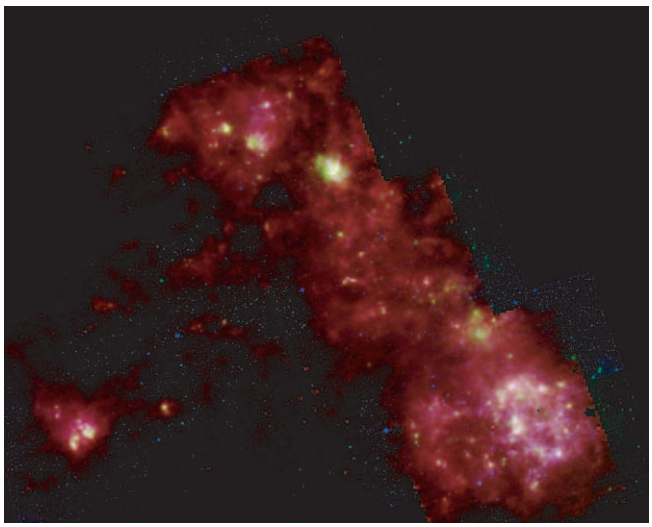

FIG. 2.—Three-color image showing the S^{3}MC maps (Bolatto et al. 2007) of the SMC at 160 μm (*red*), 24 μm (*green*), and 8 μm (*blue*). The 160 μm emission comes from BGs and extends across the whole SMC. Diffuse 24 μm emission, from hot VSGs, and the 8 μm emission, from PAHs, are both confined to the regions of active star formation.

The observed submillimeter/millimeter SED also constrains the mass of dust. We subtract the best-fit ($\beta = 2$) single-population model from the integrated spectrum and fit a single population to the residuals at long wavelengths. Assuming that this emission comes from cold dust with a Galactic emissivity ($\kappa_{250} =$ 8.5 cm^2 g^{-1} and $\beta = 2$), we find a cold dust population with $T \sim 7$ K and $M_{\rm dust} \sim 2 \times 10^6\ M_\odot$. This is very close to the minimum equilibrium temperature possible for interstellar grains ($\sim$6 K; Purcell 1969), so this represents the largest dust mass permitted by the SMC SED. Stanimirović et al. (2000) and Wilke et al. (2004) both arrive at similar values for a possible, but not necessary (see § 3.3.1), cold population, $\sim 10^6$ and $0.7 \times 10^6\ M_\odot$, respectively (for the trade-off between $T_{\rm cold}$ and $M_{\rm cold}$ see Stanimirović et al. 2000).

3.3. *The Integrated FIR SED of the SMC*

Table 3 gives the flux density integrated over the maps in the wave bands used in this paper. We also give the range of literature values, taken from Wilke et al. (2004), who present an excellent compilation of the FIR SED of the SMC. Figure 6 shows log-log and loglinear plots of flux density as a function of wavelength. In both Table 3 and Figure 6, the area considered is the whole extent of the maps in Figure 3, not just the smaller area covered by the MIPS maps. Because this is an integrated SED over a large area, we are able to include points from DIRBE and TopHat (Aguirre et al. 2003). We scale the latter by 0.9 to account for the difference between our area and the larger area studied by TopHat; this is the mean ratio of DIRBE fluxes over the TopHat area to the DIRBE fluxes over our own region. In deriving MIPS fluxes, we fill in the areas not covered by the MIPS

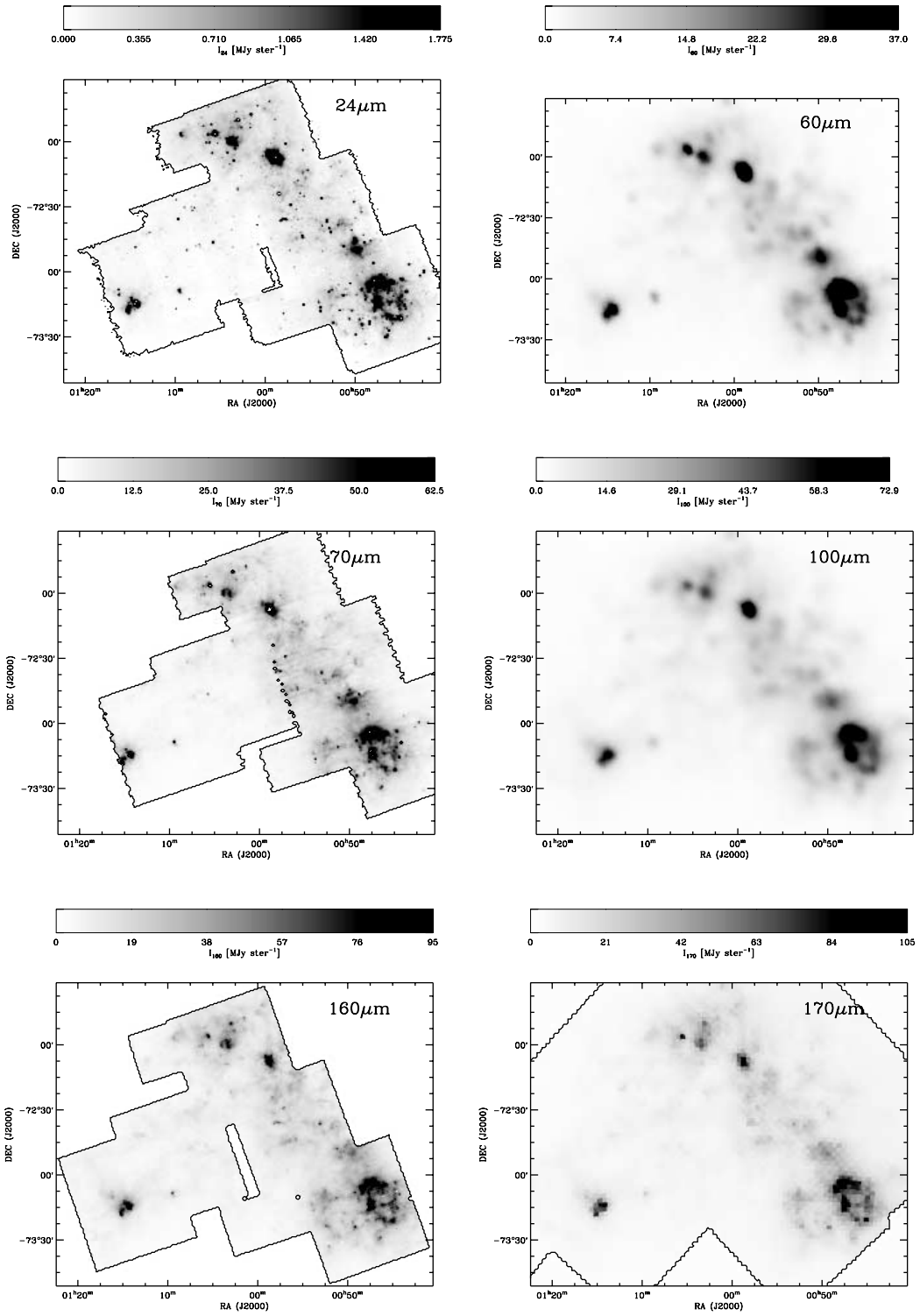

FIG. 3.—Maps of the SMC in six FIR bands arranged in order of increasing wavelength: the MIPS 24 μm map (*top left*), the IRIS 60 μm map (*top right*), the MIPS 70 μm map (*middle left*), the IRIS 100 μm map (*middle right*), the MIPS 160 μm map (*bottom left*), and the *ISO* 170 μm map (Bot et al. 2004; *bottom right*). The MIPS maps are shown at resolutions of 40″ with the extent of the map shown by a black contour. The IRIS maps have 4′ resolution. The *ISO* map has 1.5′ resolution. All six maps have been corrected for zodiacal light and the Galactic foreground. The stretch is linear with the maximum for all maps selected to be 10 times the average intensity over a common area centered on the southwest star-forming region.

maps with DIRBE data interpolated to the MIPS wave bands. These filled-in regions account for ~20% of the total flux (the MIPS maps alone yield integrated fluxes of 310, 10,000, and 15,000 Jy at 24, 70, and 160 μm, respectively).

Figure 6 and Table 3 show the photometric consistency discussed in § 2. The data for each wave band agree within the uncertainties. Figure 6 also shows the Dale & Helou (2002) models (*solid line*) and best-fit single populations with $\beta = 2$, 1.5, and 1 (*dotted, dashed, and dot-dashed lines, respectively*). All four models are derived from only the integrated 100 and 160 μm data to isolate emission from BGs. The best-fit temperature for the BGs over the whole SMC is 20.6 K, somewhat higher than the $T = 17.5$ K found for Galactic cirrus (Boulanger et al. 1996). The best-fit value for α over the whole SMC is 2.4, implying

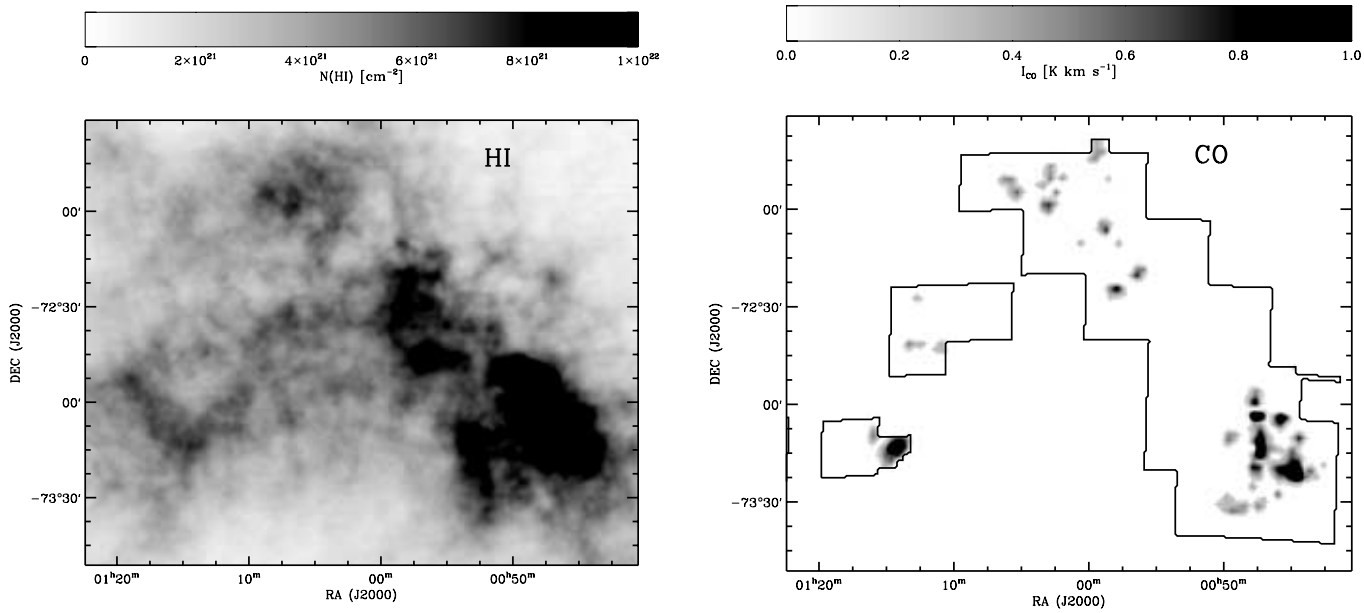

FIG. 4.—ISM in the SMC: the H I at 1.5′ resolution (Stanimirović et al. 1999; *left*), and CO intensity at 2.6′ mapped by NANTEN (Mizuno et al. 2001; N. Mizuno et al. 2007, in preparation; *right*). The black contour shows the extent of the NANTEN survey.

cirrus-like medium with a mean radiation field close to the solar neighborhood value.

3.3.1. *The Long-Wavelength Emission*

The SMC emits more at submillimeter and millimeter wavelengths than one would estimate from the FIR emission assuming Galactic dust ($\beta = 2$). This may be typical for a dwarf irregular galaxy (Bolatto et al. 2000b; Lisenfeld et al. 2002; Galliano et al. 2005). This long-wavelength emission may indicate the presence of cold dust invisible in the FIR (Stanimirović et al. 2000; Aguirre et al. 2003; Wilke et al. 2004); therefore, its interpretation is relevant to this work. If the long-wavelength emission is due only to cold dust with a Galactic $\beta = 2$, then it could have $T_{\rm cold} \sim 7$ K and $M_{\rm cold} \sim 2 \times 10^6\ M_\odot$, representing the dominant component of both dust and heavy elements in the SMC. Galliano et al. (2005) argued for this in several galaxies similar to the SMC: that very cold (5–9 K) dust makes up 40%–80% of the dust mass.

However, Figure 6 shows that the long-wavelength emission can also be explained by an emissivity power-law index shallower

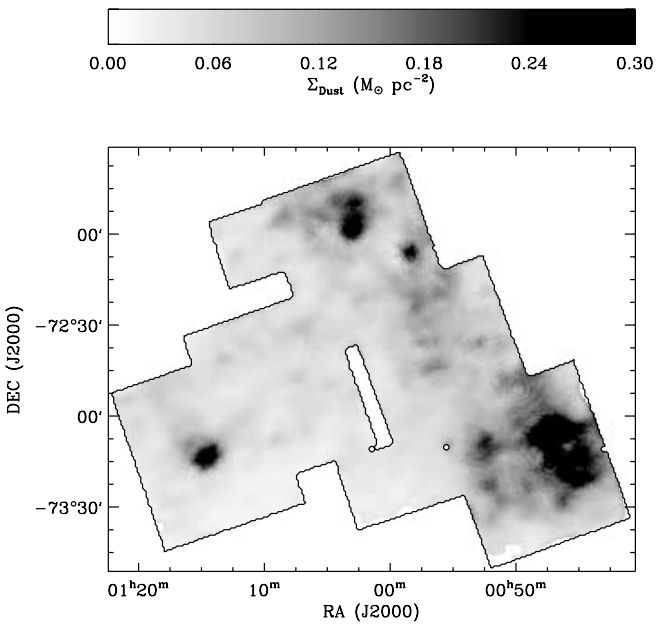

FIG. 5.—Dust mass surface density map for the SMC at 4′ resolution. The black line shows the extent of the MIPS 160 μm map.

TABLE 3
INTEGRATED SED OF THE SMC

Wave Band (μm)	Data Set	Flux Density (Jy)
24	MIPS	350 ± 50
25	Literature[a]	256–460
	HIRAS	270 ± 40
	IRIS	360 ± 60
	DIRBE	310 ± 50
60	Literature[a]	6689–8450
	HIRAS	7700 ± 1300
	IRIS	7400 ± 1300
	DIRBE	7200 ± 1300
70	MIPS	12500 ± 2400
100	Literature[a]	12650–16480
	HIRAS	15500 ± 2200
	IRIS	14500 ± 2300
	DIRBE	15600 ± 2500
140	Literature[a]	14000–20030
	DIRBE	16600 ± 4700
160	MIPS	19000 ± 4300
170	Literature[a]	15000 ± 2300
	ISO	18500 ± 4000
240	Literature[a]	9600–12070
	DIRBE	10700 ± 3200
476	TopHat[b]	2800 ± 800
652	TopHat[b]	1400 ± 300
750	TopHat[b]	840 ± 200
1224	TopHat[b]	280 ± 80

[a] The range of values from the literature compiled by Wilke et al. (2004) from Schwering (1988), Rice et al. (1988), Stanimirović et al. (2000), Wilke et al. (2003), and Aguirre et al. (2003).

[b] Fluxes from TopHat scaled to our common area. The total fluxes from Aguirre et al. (2003) are 3200, 1620, 950, and 320 Jy.

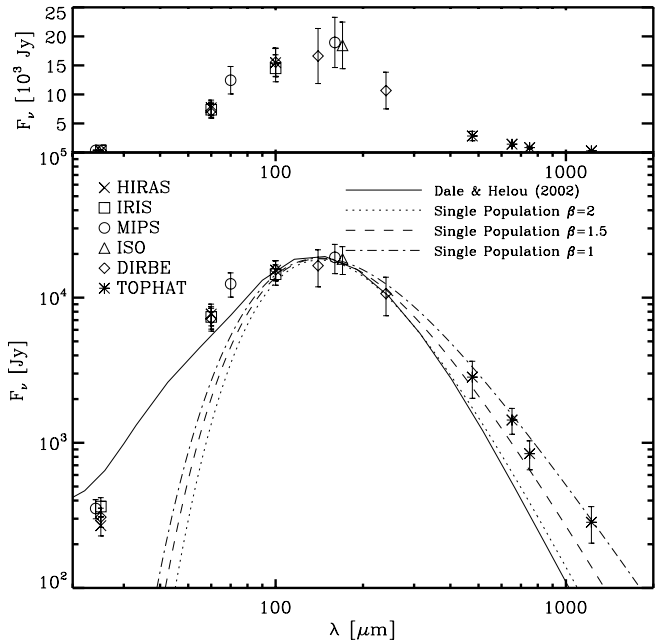

FIG. 6.—Integrated SED of the SMC over the region shown in Fig. 3 on linear (*top*) and logarithmic (*bottom*) scales. We use DIRBE to fill in the (low intensity) regions beyond the coverage of the MIPS maps. We scale the TopHat data (Aguirre et al. 2003) by 0.9 to match the area we consider. The photometric consistency among the various bands is good. Nearby bands agree within 1 σ in all cases. The solid line shows the best-fit Dale & Helou (2002) model, derived from the 100 and 160 μm fluxes. The three dotted lines show a single dust population with a temperature inferred from the 100 μm–to–160 μm color and emissivity power laws with $\beta = 2$, 1.5, and 1.

than $\beta = 2$ and little or no cold dust. The best fit to the FIR adopting $\beta = 1.5$ yields fluxes within 2 σ of every TopHat data point, although still systematically low. The best-fit β from 100 μm to 1 mm with a single population is $\beta \approx 1$ (Aguirre et al. [2003] find $\beta = 0.91$). Values of $\beta = 1$ and 1.5 are within the range of plausible astrophysical values, being appropriate for amorphous carbon and silicate grains, respectively. Because the dust in the SMC is believed to be dominated by silicate grains, a value of $\beta = 1.5$ may be more appropriate than $\beta = 2.0$. Indeed, the best-fit β to the long-wavelength values $\kappa_{\rm abs}$ found by Weingartner & Draine (2001) and Li & Draine (2001, 2002) for SMC grains beyond $\sim$300 μm is 1.65. Further, Alton et al. (2004) argue that $\beta = 1.5$ describes emissivity determinations from the literature as well as or better than $\beta = 2.0$.

Lisenfeld et al. (2002, 2005) observed similar long-wavelength emission in NGC 1569, an irregular galaxy similar to the SMC in mass. They suggest that the small, hot grains responsible for the 24–70 μm emission may also cause the long-wavelength emission. Using a modified version of the Désert et al. (1990) models, they showed that an SED dominated by VSG emission (with no PAHs) can fit the data as well as a model containing cold BGs. They argue that NGC 1569, a metal-poor galaxy with a strong interstellar radiation field, is an unlikely locale to find a large amount of dust at unusually low temperatures. While such dust might hide in a few molecular regions across the galaxy (we identify likely spots for this in the SMC below), there is a dearth of places to hide the truly large amount of dust needed to account for the long-wavelength emission. Further, if such a reservoir of hidden dust does exist, it necessarily means that the metallicity of these galaxies has been underestimated, in some cases substantially. On the other hand, in a dynamically active environment with poor shielding, an enhancement of VSGs relative to BGs may be expected as enhanced erosion dust particle mantles turn BGs into VSGs. These arguments may also apply to the SMC. However, the 25 μm/60 μm and 60 μm/160 μm colors in NGC 1569 ($\approx$0.13 and 1.2) are higher than in the SMC ($\approx$0.05 and 0.4), more consistent with the hypothesis of a large population of very hot dust. Simultaneous fitting of the IRAC, MIPS, and *IRAS* data will be presented in a future paper.

Resolved submillimeter data are crucial to address the most compelling question raised by Lisenfeld et al. (2002, 2005): where, spatially, is the millimeter emission coming from? The Aguirre et al. (2003) results, with a beam of several degrees, cannot address this question. At present, only one SMC molecular cloud has published, resolved mapping at millimeter wavelengths. This is SMC B1 No. 1, mapped by SEST at 1.2 mm (Rubio et al. 2004). Toward this cloud, we measure a background-subtracted flux of $F_{\rm B1,160} \approx 1.5$ Jy.[7] Rubio et al. (2004) find $F_{\rm B1,1200} = 50 \times 10^{-3}$ Jy. Therefore, $F_{160}/F_{1200} \approx 30$ for SMC B1 No. 1 compared to $F_{160}/F_{1200} \approx 65$ for the global SED (see § 3.3). This GMC, described by Rubio et al. (2004) as cold and quiescent, shows a millimeter excess relative to the whole SMC, consistent with a cold dust temperature. However, the excess is too small to explain the observed emission; extrapolating from SMC B1 No. 1 ($\sim$1% of the CO luminosity) to the whole SMC yields a millimeter flux of only a few janskys. Aguirre et al. (2003) measure 280 ± 80 Jy at $\lambda = 1.2$ mm.

We present three explanations for the long-wavelength emission: a wealth of cold dust, an abundance of hot small grains, and an emissivity law that differs from the Galactic one. We cannot rule out any of these, but we prefer the latter, a modified emissivity, because it is simple and because the available FIR/CO/millimeter data provide some evidence against the first and second explanations.

3.4. *Molecular Gas Map*

If dust and gas remain well mixed over the $\sim$400 pc scales of our calibration regions and the properties of grains do not vary too dramatically from the atomic to the molecular ISM, then the dust can be an optically thin tracer of molecular gas. Dust measured from FIR emission offers several key advantages over traditional molecular line tracers: unlike CO emission, dust emission is optically thin; unlike molecules, dust is not expected to be preferentially destroyed relative to H_2 in the outer parts of molecular clouds (e.g., Maloney & Black 1988); and the abundance of dust relative to gas may be directly measured elsewhere in the galaxy via comparison with the H I, while the use of molecular lines as tracers of gas must be calibrated within the GMCs themselves. In this section we use a method adapted from Israel (1997b) and Dame et al. (2001) to construct a map of the H_2 in the SMC. We summarize the method, present the map, and then discuss the uncertainties associated with the map.

3.4.1. *Method and Map*

To measure the H_2 mass surface density, $\Sigma_{\rm H_2}$, along a line of sight, we first adopt a dust-to-hydrogen ratio, D/H. We apply D/H to the dust mass surface density to estimate the total (atomic plus molecular) mass surface density along the line of sight, $\Sigma_{\rm total}$. This is

$$\Sigma_{\rm total} = \Sigma_{\rm H\,I} + \Sigma_{\rm H_2} = \frac{\Sigma_{\rm dust}}{\rm D/H}. \quad (3)$$

[7] In a 1.5′ radius aperture about $\alpha_{\rm B1950.0} = 0^{\rm h}43^{\rm m}42.4^{\rm s}$, $\delta_{\rm B1950.0} = -73^\circ35'10''$ (Rubio et al. 1993), with the background measured from an annulus between 5′ and 6′ to avoid contamination.

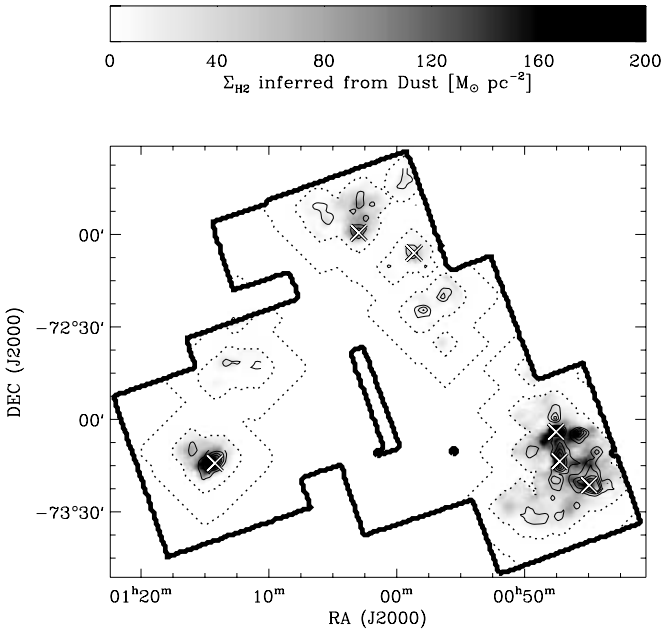

FIG. 7.—Illustration of the methods used to construct the map of Σ_{H_2} shown in Fig. 8. Thin black contours show CO emission (at 0.3, 0.6, 0.9, and 1.2 K km s^{-1}), used to select regions over which we measure Σ_{H_2}. Dotted contours show the boundary of the reference regions (merged together) over which we measure local values of D/H. We calculate Σ_{H_2} only within the inner dotted boundary; the reference region is free of H_2 by construction. Crosses indicate selected peaks from both the CO and H_2 maps that will be used below. The gray scale shows the derived Σ_{H_2}.

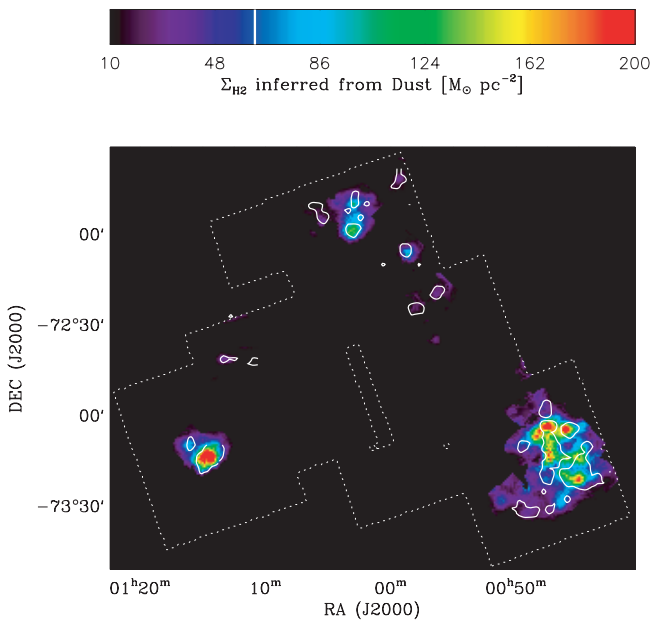

FIG. 8.—Color image showing molecular gas mass surface density in the SMC inferred from the dust, from 10 to 200 $M_\odot$ pc^{-2}. The 1 σ uncertainty in Σ_{H_2} is $\sigma_{\Sigma H_2} \approx 6\ M_\odot$ pc^{-2}. The contours show the extent of significant (3 σ) CO emission, which is 0.3 K km s^{-1}, or $\approx$62 $M_\odot$ pc^{-2} at $X_{CO} = (13 \pm 1) \times 10^{21}$ cm^{-2} (K km s^{-1})$^{-1}$ (see § 4.2.1). Both maps are at the 2.6′ resolution of the CO map. The dashed white contour shows the extent of the MIPS 160 μm map.

We remove the H I column, $\Sigma_{H\,I}$, from each line of sight to get a molecular gas column, $\Sigma_{H_2} = \Sigma_{total} - \Sigma_{H\,I}$. We measure $\Sigma_{H\,I}$ from the map by Stanimirović et al. (1999), which includes zero spacing data. Thus,

$$\Sigma_{H_2} = \frac{\Sigma_{dust}}{D/H} - \Sigma_{H\,I}. \quad (4)$$

We measure D/H by comparing the mass surface density of dust (Fig. 5) to the mass surface density of H I over a series of reference regions, attempting to simultaneously satisfy two conditions: (1) that the reference regions are free of molecular hydrogen, and (2) that the reference measurement take place near the region where we want to determine Σ_{H_2}, in order to minimize the effect of spatial variations in D/H. We adopt the following method:

1. We identify regions likely to contain molecular gas from the CO map (Mizuno et al. 2001; N. Mizuno et al. 2007, in preparation). This is all lines of sight within 3.6′ (65 pc) of 3 σ CO emission. We derive Σ_{H_2} over each of these regions.
2. For each region, we create a reference region over which we measure D/H. This is all lines of sight more than 3.6′ (65 pc) away from the CO but nearer than 10.8′ (200 pc). The reference region is close enough that D/H should apply to the H_2, but distant enough that contamination by H_2 is unlikely. We check this by stacking CO spectra across all of our reference regions: we measure $\bar{I}_{CO} \approx 0.04$ K km s^{-1}, so there is only very diffuse CO emission in the reference region (compare to $\bar{I}_{CO} \approx 0.12$ K km s^{-1} in the region outside of 3 σ CO but within 65 pc).
3. Over each reference region, we measure the mean D/H and derive Σ_{H_2} using equation (4).

Figure 7 illustrates this method. We show a map of the derived Σ_{H_2}, the CO emission (*black contours*), and an outline of the set of all reference regions (*dotted contours*). Crosses mark peaks in the H_2 and CO distributions (used below).

In order to match the resolution of the CO map, we derive Σ_{H_2} from a high-resolution version of our dust map. We measure the 100 μm–to–160 μm ratio at the IRIS resolution, but we derive the dust surface density (given the color) from the MIPS 160 μm map at the CO resolution. We assume that the colors measured at 4′ resolution apply to the map at 2.6′ resolution. We performed the same calculation using the HIRAS 100 μm map, which has a 1.7′ resolution. We derive a comparable H_2 mass, but the map has a number of artifacts with scales comparable to GMCs and therefore offers a check but no improvement.

Figure 8 shows the molecular gas mass surface density, Σ_{H_2}, derived using this method. The white contours indicate the extent of 3 σ significant CO emission (0.3 K km s^{-1}; Mizuno et al. 2001; N. Mizuno et al. 2007, in preparation) assuming the average X_{CO} we derive below [$(13 \pm 1) \times 10^{21}$ cm^{-2} (K km s^{-1})$^{-1}$]. The H_2 map contains a total of $3.2 \times 10^7\ M_\odot$ of molecular hydrogen. We estimate the plausible range of H_2 masses given our systematic uncertainties as $\approx$(1.5–4.0) $\times 10^7\ M_\odot$.

3.4.2. *Uncertainties and Systematics*

The statistical uncertainty in Σ_{H_2} is small, only $\approx 6\ M_\odot$ pc^{-2}. We estimate this from the measured uncertainties in Σ_{dust} and D/H and confirm it in two ways: (1) by introducing noise at the 8% level (see Appendix B) into Σ_{dust} and deriving new Σ_{H_2} maps for many realizations, and (2) by computing Σ_{H_2} for several regions known to be free of CO emission. We also check the zero level in these empty regions, finding -5 to 0 $M_\odot$ pc^{-2}.

Systematic uncertainties in the FIR maps (foreground, calibration, and saturation) will propagate to Σ_{H_2}. To evaluate these, we offset the 100 and 160 μm maps by ± 1 MJy sr^{-1} one at a time and rederive Σ_{H_2}. We perform similar tests to test the effect of our calibration and saturation; we scale first the whole 160 μm map and then just the bright regions by 1.25. Over all tests we

find M_{H_2} in the range $(1.4–3.9) \times 10^7\ M_\odot$, suggesting a ~50% uncertainty.

We avoid several systematic uncertainties by performing the determination of the D/H locally for each region. Nonetheless, several astrophysical uncertainties may affect Σ_{H_2}: the choice of dust map, changes in dust properties between the atomic and molecular ISM, and the possibility of hidden cold dust.

The uncertainty in Σ_{H_2} associated with our choice of a particular dust map is less than 30%. We estimate this using test maps adopting the various options described in Appendix B (i.e., single population, only the 60 and 100 μm data, etc.). The total H_2 inferred from resulting maps spans $M_{H_2} = (2.1–3.2) \times 10^7\ M_\odot$, with most values in the range $(2.4–3.2) \times 10^7\ M_\odot$. Note that applying this method directly to the MIPS 160 μm intensity alone yields $M_{H_2} = 3.8 \times 10^7\ M_\odot$.

Dust properties, especially the FIR opacity and D/H, may vary between the atomic and molecular ISM, primarily due to growth of icy mantles on the surfaces of dust grains in GMCs. These effects have the sense of decreasing Σ_{H_2} and a magnitude as high as a factor of 2–3, although this must be considered an upper limit because conditions in the SMC H_2 will be less conducive to the growth of icy mantles than in Milky Way GMCs. See § 4.1 for more details.

If the possible population of very cold dust discussed in § 3.3.1 exists, our Σ_{dust} map will be incomplete. If cold dust is concentrated in GMCs, we will underestimate Σ_{dust} and thus Σ_{H_2} in these regions. In this case Σ_{H_2} and Σ_{dust} represent only lower limits. However, a large amount of cold dust is not required to explain the SED (§ 3.3.1), and indeed we consider it unlikely. In § 4.2.2 we find that quiescent gas with a high CO-to-FIR ratio represents ≈30% of the CO emission in the SMC. If we allow that we miss all of H_2 associated with these clouds in our map and assume that the average X_{CO} we measure holds across the SMC, cold dust will represent a ~30% correction to the overall H_2 mass.

Table 4 lists the uncertainties discussed here and gives our estimate of the maximum magnitude for each effect. Israel (1997a) gives a more thorough discussion of the uncertainties associated with this method. He concludes that most uncertainties have the effect that we underestimate the true H_2 mass. We noted two exceptions, increased FIR opacity and D/H in GMCs, above. Another is that we might mistakenly bookkeep warm ionized gas as H_2. This requires very good resolution to investigate and so remains uncertain. However, studying the Eridanus superbubble, Heiles et al. (1999) found that IR not associated with H I is mainly associated with H_2, not ionized gas.

Several arguments suggest that our map of Σ_{H_2} is not dominated by these systematics. Most importantly, Dame et al. (2001) found that H_2 estimated from FIR and CO emission agree well in the Milky Way, so the method we apply to the SMC works in the Galaxy. The estimate of X_{CO} that Dame et al. (2001) derive using this method is $1.8 \times 10^{20}\ \mathrm{cm^{-2}\ (K\ km\ s^{-1})^{-1}}$, in excellent agreement with estimates based on gamma rays (Strong & Mattox 1996). Further, Schnee et al. (2006) studied the relation between FIR emission and dust column for a simulated turbulent, externally heated cloud. They found that the 100 μm/240 μm color (the best analog to our 100 μm/160 μm) does a good job of matching the extinction for $A_V \lesssim 4$, although it may underpredict the dust content above that value. Finally, Figure 8 shows good agreement between our H_2 map and the CO map, particularly toward regions of active star formation. In fact, toward these regions the H_2 is more extended than CO, suggesting that when dust is warm enough to emit in the FIR, the dust may trace H_2 better than CO.

Our estimate of the likely uncertainty in the Σ_{H_2} map is 50%. Systematic uncertainties in the data, dust modeling, and a modest population of cold dust are all important, but many of these effects have offsetting senses.

TABLE 4
Uncertainties in the Σ_{H_2} Map

Description	Sense	Magnitude
Data:		
Statistical[a]	±	6 $M_\odot$ pc^{-2}
Foreground	±	$^{+10\%}_{-30\%}$
Calibration	−	30%
Saturation	+	10%
H_2 in reference region	+	20%
Astrophysical:		
Model for dust map	−	30%
Icy mantle growth in GMCs	Divide	$(2–3) f_{cold}$[b]
Cold dust (best guess)	+	30%
Cold dust (maximum)	+	Σ_{H_2} is a lower limit

[a] Per line of sight.
[b] The fraction of molecular gas cold enough that accretion onto grains is significant, which we argue to be small.

4. ANALYSIS

4.1. *Dust and Atomic Gas*

Over the region of the MIPS 160 μm map, the SMC has an H I mass of $M_{H\,I} = 1.8 \times 10^8\ M_\odot$. The remainder of the $4 \times 10^8\ M_\odot$ of H I associated with the SMC (Stanimirović et al. 1999) lies in an extended component not covered by the MIPS map. With $M_{dust} = 3 \times 10^5\ M_\odot$, this implies $\log_{10}(\mathrm{D/H\ I}) = -2.78$, or 1:600 over the whole SMC. If we include $M_{H_2} \approx 3 \times 10^7$, then $\log_{10}(\mathrm{D/H}) = -2.86$, or 1:700. Including helium, the total DGR is $\log_{10}\mathrm{DGR} \approx -3.0$. This is lower than the DGR in the Milky Way by about the same factor as the metallicity difference between the two systems with an uncertainty of a factor of ~2 (see Appendix B). This result is consistent with measurements by Bouchet et al. (1985), who found a reddening per gas column $\sim\frac{1}{8}$ Galactic, and by Wilke et al. (2004), who found a DGR of 1:540. There are several predictions for how the DGR varies with Z. If we formulate DGR $\propto Z^a$, then Issa et al. (1990) find $a = 1.2$, Schmidt & Boller (1993) find $a = 1.6$, Lisenfeld & Ferrara (1998) find $a = 1.9$, and Dwek (1998) finds $a = 1.3$. These fits predict $\log_{10}\mathrm{DGR} \approx -3.0$, -3.0, -3.3, and -3.5. We cannot rule out any of these values, but our derived DGR leads us to prefer the shallower Issa et al. (1990) and Dwek (1998) fits.

Figures 9 and 10 compare dust and *atomic* gas in our maps. Figure 10 shows that dust surface density and atomic gas surface density are correlated across the SMC, with a rank correlation coefficient $r_k \sim 0.76$ across all data. Both figures show that the D/H I is a function of location in the SMC (previously noted by several authors and shown nicely in profile by Stanimirović et al. 2000). Diffuse gas in the wing, distinguished by a simple intensity cut, $I_{160} > 10$ MJy sr^{-1} (which is arbitrary but does a good job), shows a low mean $\log_{10}(\mathrm{D/H\ I_{wing}}) = -2.94 \pm 0.02$, while for the bar $\log_{10}(\mathrm{D/H\ I_{bar}}) = -2.71 \pm 0.01$, a factor of 2 higher. Lines of sight toward regions with CO emission show higher D/H I than nearby lines of sight; the mean is $\log_{10}(\mathrm{D/H\ I_{CO}}) = -2.54 \pm 0.02$. It is therefore possible to identify most of the SMC star-forming regions from the map of D/H I, Figure 9.

Some of the variations in D/H I may be understood in terms of the life cycle of dust. Dwek (1998) outlines a picture in which dust is depleted in supernova shocks and accretes new material within molecular clouds. Bot et al. (2004) argued that supernova shocks will destroy dust more easily in the diffuse gas found in

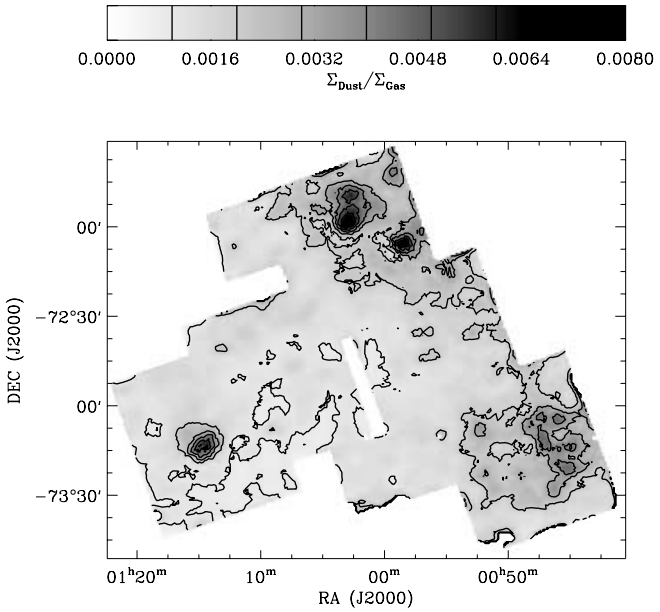

FIG. 9.—Ratio of dust mass surface density to atomic gas mass surface density at 4′ resolution. Star-forming regions show very high DGRs, probably because they contain molecular gas, which is not accounted for in this map. The star-forming bar of the SMC shows higher D/H I than the diffuse wing.

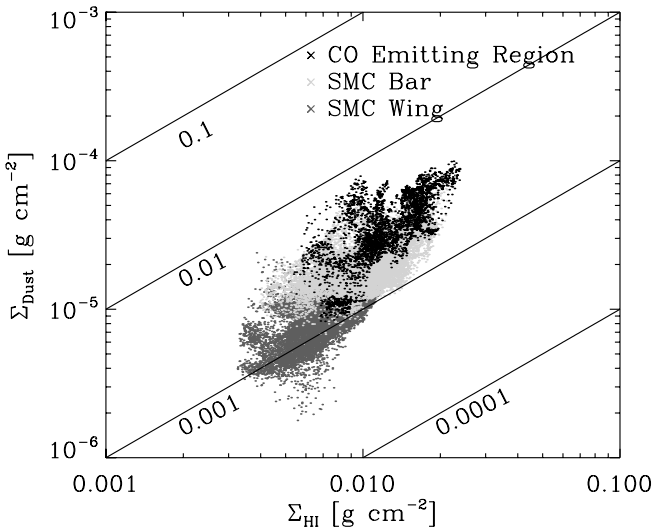

FIG. 10.—Dust surface density as a function of H I surface density. Lines of sight toward CO emission, the SMC bar, and the low-intensity wing are marked with black, light gray, and dark gray dots, respectively. Lines of constant DGR are labeled. The correlation between dust surface density and H I is good across the SMC. The bar shows a higher D/H I than the wing, and regions near CO emission show the highest DGRs, probably because they harbor significant amounts of molecular gas.

the wing. Sembach & Savage (1996) observed a similar effect in the Milky Way, that depletion of some elements decreases with increasing distance from the plane of the Galaxy. This effect, combined with the distance from the sources of new dust in the bar, may explain the enhanced depletion in the wing.

The values of the D/H I near CO emission must be due, at least in part, to the presence of molecular gas; the presence of CO emission necessitates some H_2 along the line of sight. If this is the dominant effect, then H_2 accounts for ~30% of the gas surface density in these regions, on average. The processing of dust inside GMCs may also contribute to the high $\log_{10}$(D/H $_{CO}$): accretion of heavy elements onto grains may result in an enhanced dust abundance and higher FIR opacities.

Dwek (1998) estimates that over the lifetime of a Milky Way GMC, the dust mass in the cloud may increase by a factor of 2–3 due to accretion of heavy elements (see also references therein); so for a Milky Way GMC in the middle of its lifetime, we would expect an enhancement in the DGR of ~1.5–2. However, an observational measure of the average DGR enhancement between the diffuse and molecular ISM is hard to come by. In the Milky Way, Rachford et al. (2002) found gas and dust to be well mixed along lines with $A_V \gtrsim 1$. There is some evidence from absorption studies that the DGR varies in the SMC with higher values toward lines of sight with more H_2 (Sofia et al. 2006), but the sample is too small to evaluate the significance of this finding.

Some of the enhanced D/H $_{CO}$ may also result from dust in GMCs having larger FIR emission per unit mass at a given temperature (i.e., higher κ_{FIR}). In the Milky Way, dust associated with dense, colder gas is observed to have a higher emissivity than diffuse, warm gas (Cambrésy et al. 2001; Stepnik et al. 2003). Modeling the effect of icy mantles on grains in protostellar cores, Ossenkopf & Henning (1994) found an enhancement of a factor of 2–3 in the FIR opacity.

Both of these effects depend on conditions found at high A_V, which may be more common in Milky Way GMCs than in the SMC. We see below that $A_V \sim 1$–2 is typical for an SMC GMC, ~3 times less on average than for Milky Way GMCs. Therefore, these conditions will not be as prevalent in SMC H_2 as in the Milky Way. If DGR enhancements and increased κ_{FIR} are important effects, then the true A_V toward SMC GMCs is even lower. Therefore, we argue that the factors of 2–3 discussed here for both effects must be viewed as upper limits. In particular, the Ossenkopf & Henning (1994) calculations are for cores with densities $\gtrsim 10^5$ cm^{-3}, which will represent only a tiny fraction of the molecular gas in the SMC. While all three effects contribute to the high value of D/H $_{CO}$, we consider it likely that the presence of H_2 is primarily responsible for the high D/H $_{CO}$.

4.2. CO *and* H_2 *in the SMC*

4.2.1. *The* CO-*to*-H_2 *Conversion Factor*

Our H_2 map contains 3.2×10^7 $M_\odot$ of molecular hydrogen. The CO luminosity in the Mizuno et al. (2001) and N. Mizuno et al. (2007, in preparation) NANTEN map over the same area is 1.5×10^5 K km s^{-1} pc^{-2} (summing over the entire map without masking). This implies a mean CO-to-H_2 conversion factor, X_{CO}, of $(13 \pm 1) \times 10^{21}$ cm^{-2} (K km s^{-1})$^{-1}$, which is 65 times the Galactic value. This conversion factor varies systematically within the SMC. Regions with high CO intensity ($I_{CO} > 0.3$ K km s^{-1}) have $X_{CO} = (9 \pm 1) \times 10^{21}$ cm^{-2} (K km s^{-1})$^{-1}$, while regions with diffuse CO emission ($I_{CO} < 0.3$ K km s^{-1}) have twice this value, $X_{CO} = (18 \pm 2) \times 10^{21}$ cm^{-2} (K km s^{-1})$^{-1}$.

If CO and H_2 are not coincident (see § 4.2.2), then we must be careful in defining exactly what is meant by the CO-to-H_2 conversion factor. Indeed, much of the controversy in the literature is caused by confusing large spatial scale conversion factors, which may include H_2 without associated CO, with local conversion factors, which are limited to regions with substantial CO emission. Therefore, we calculate a refined value of X_{CO} over the common volume shared by CO and H_2 for the molecular peaks marked in Figure 7. We compare CO emission to H_2 in a 1′ diameter aperture, essentially measuring the beam pointed at the center of the cloud. We then adjust the H_2 down by a factor of 1.3 to account for H_2 along the line of sight that lies outside of the CO-emitting region (we find in § 4.2.2 that the H_2 is more extended than the CO by this factor). Table 5 shows the results. We

TABLE 5
PROPERTIES OF SEVERAL MOLECULAR PEAKS

α (J2000.0)	δ (J2000.0)	$\Sigma_{H\,I}$ ($M_\odot$ pc^{-2})	Σ_{H_2} ($M_\odot$ pc^{-2})	X_{CO}[a] [10^{21} cm^{-2} (K km s^{-1})$^{-1}$]	HWHM(H_2) (pc)	HWHM(CO) (pc)	$\log_{10}$(D/H) (Reference)
01 13 45.8	−73 16 30	58	261	7.1	40	36	−2.93
01 02 49.3	−72 02 51	49	133	10	44	33	−2.70
00 58 54.8	−72 09 24	36	81	5.4	35	22	−2.64
00 48 10.4	−73 06 03	106	230	5.6	53	22	−2.82
00 47 46.4	−73 15 34	83	162	4.0	69	26	−2.82
00 45 26.2	−73 22 45	70	199	6.5	40	54	−2.82

NOTE.—Units of right ascension are hours, minutes, and seconds, and units of declination are degrees, arcminutes, and arcseconds.
[a] Applying a correction of 1/1.3 to account for H_2 beyond the CO along the line of sight (see text).

find a mean $X_{CO} = (6 \pm 1) \times 10^{21}$ cm^{-2} (K km s^{-1})$^{-1}$. We derive a similar value, $X_{CO} = (7 \pm 1) \times 10^{21}$ cm^{-2} (K km s^{-1})$^{-1}$, by considering lines of sight with bright CO ($I_{CO} > 0.6$ K km s^{-1}) and scaling by the radius ratio (1.3). Because it represents our best estimate of X_{CO} over the volume from which the CO emission originates, this is the value most directly comparable to virial mass estimates.

Table 6 summarizes X_{CO} from this paper and the literature. Most of these values are from virial mass measurements, which obtain values of X_{CO} that are systematically higher than the Galactic value but dependent on the scale of the structure studied (Rubio et al. 1993; Bolatto et al. 2003). Larger structures yield higher values of X_{CO}. Indeed, Bolatto et al. (2003), studying the N83/N84 region, found nearly Galactic values of X_{CO} when considering the smallest resolved structures in their data set (GMCs with radii of 10–20 pc) but at the scale of the entire complex found a conversion factor ~10 times the Galactic value. At a common scale of ~40–100 pc, the virial mass method yields $X_{CO} = (0.9–3.5) \times 10^{21}$ cm^{-2} (K km s^{-1})$^{-1}$. At the same scales, our FIR-based H_2 map yields $X_{CO} \approx (6 \pm 1) \times 10^{21}$ cm^{-2} (K km s^{-1})$^{-1}$, 2–6 times higher.

The discrepancy between M_{H_2} measured from the FIR and the virial mass may be explained if magnetic fields may provide most of the support for SMC GMCs. Magnetic support will not affect the turbulent line width, so in this case the virial mass will underestimate the true mass of the GMC (e.g., McKee & Zweibel 1992). C. Bot et al. (2007, in preparation) compare H_2 masses estimated from millimeter emission to CO-based virial masses for a set of SMC and Milky Way GMCs. They find that in Milky Way clouds the virial mass usually exceeds the millimeter-based mass, but that SMC clouds have higher millimeter masses than virial masses. They attribute this difference to enhanced support by magnetic fields in SMC clouds. If magnetic support does not play an important role, SMC clouds may be short-lived as this measurement implies that the kinetic energy is much smaller than the gravitational potential energy.

Israel (1997b) applied a method similar to ours to estimate M_{H_2} toward several regions in the SMC with a limiting resolution of 15′ (~270 pc). Given this resolution, his value of $X_{CO} = (12 \pm 2) \times 10^{21}$ cm^{-2} (K km s^{-1})$^{-1}$ is best compared to our global value, $(13 \pm 1) \times 10^{21}$ cm^{-2} (K km s^{-1})$^{-1}$, and the two are identical within the uncertainties. Application of his method to the newer data used in this paper yields $X_{CO} = (9–13) \times 10^{21}$ cm^{-2} (K km s^{-1})$^{-1}$ for lines of sight with CO emission, depending on the method used to define reference regions. The similarity between our results using the 100 and 160 μm bands and the Israel (1997b) results using the *IRAS* 60 and 100 μm bands shows that a color-corrected 100 μm map is enough to capture the gross behavior of H_2 in a galaxy. This is also seen by the success of Dame et al. (2001) in matching Galactic FIR emission to the CO distribution. Longer wavelength (especially submillimeter) data may improve the accuracy of column density estimates by ~10% and reduce the scatter substantially (Schnee et al. 2006) but are not necessary to obtain the basic result. The improvements in the Σ_{H_2} map presented here are chiefly as follows: resolution capable of distinguishing Galactic GMCs (~50 pc), allowing us to study the relative structure of CO and H_2; and the use of local reference regions to calibrate out variations in D/H across the SMC—the low resolution of Israel (1997b) made a single D/H appropriate for that work.

TABLE 6
CO-TO-H_2 CONVERSION FACTOR

Source	X_{CO} [cm^{-2} (K km s^{-1})$^{-1}$]
Whole SMC[a]	$(13 \pm 1) \times 10^{21}$
LOS $I_{CO} > 0.3$ K km s^{-1}[a]	$(9 \pm 1) \times 10^{21}$
LOS $I_{CO} < 0.3$ K km s^{-1}[a]	$(18 \pm 2) \times 10^{21}$
Molecular peaks[a,b]	$(6 \pm 1) \times 10^{21}$
Mizuno et al. (2001)[c]	$(1–5) \times 10^{21}$
Blitz et al. (2007)[c]	$(0.9–1.5) \times 10^{21}$
Rubio et al. (1993)[c]	$9.0 \times 10^{20} (R/10\ \mathrm{pc})^{0.7}$
Bolatto et al. (2003):[c]	
Individual GMCs	$(1.8–7.8) \times 10^{20}$
N83/N84 complex	2.2×10^{21}
Israel (1997b)[a,d]	1.2×10^{22}
Rubio et al. (2004)[e]	$(1.3–3.6) \times 10^{22}$

[a] Using FIR to trace H_2.
[b] Marked in Fig. 7. Adjusted by 1.3 to account for extended H_2 beyond CO along the line of sight. Most appropriate for comparison with the virial mass.
[c] Using virial mass method.
[d] Using *IRAS* 60 and 100 μm bands.
[e] Submillimeter continuum observations.

4.2.2. *Comparison between* H_2 *and* CO

Figure 8 shows that CO predicts the presence of H_2 almost perfectly. However, the reverse is not true; we derive substantial H_2 surface densities beyond the 3 σ CO emission (*white contours*). Thus, H_2 appears more extended than CO emission in SMC star-forming regions. However, an alternative explanation is hard to rule out: because X_{CO} is very high, the surface density sensitivity of the CO map may in fact be quite poor. In this case, there may be low-intensity CO below the noise level of the map and the differences in the area are an artifact of sensitivity. In this section we show that these differences are more than a sensitivity effect; there are substantial variations in X_{CO} across the SMC.

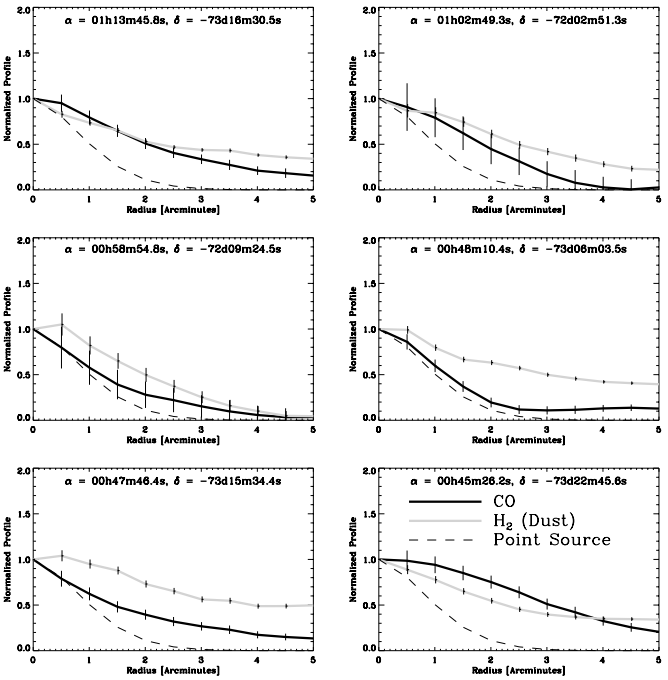

FIG. 11.—Normalized CO intensity (*black*) and H_2 surface density (*gray*) in concentric rings around selected maxima. All profiles are normalized to the central value and then averaged in concentric rings. The dashed lines show the profile of a point source. The H_2 profile derived from the FIR and H I is more extended than the CO emission in four of six cases; in the other two cases the profiles are comparable. The position of each maximum is indicated at the top of the panel, and the maxima are noted with green crosses in Fig. 8.

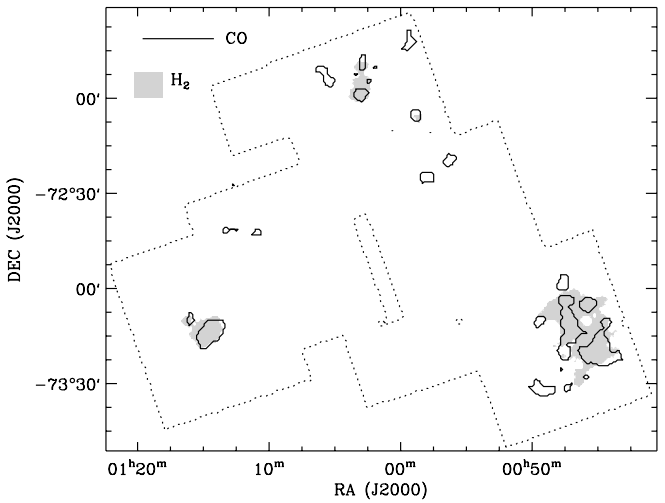

FIG. 12.—Extent of CO and H_2 from the FIR at a common significance assuming our global CO-to-H_2 conversion factor, $X_{CO} = (13 \pm 1) \times 10^{21}$ cm^{-2} (K km s^{-1})$^{-1}$. Both maps are clipped at the 3 σ for the CO, or $\Sigma_{H_2} \approx 60\,M_\odot$ pc^{-2}. In regions of active star formation, the H_2 shows a greater extent than the CO, but away from these regions, CO emission may indicate the presence of cold(er) dust.

Figure 11 shows the distribution of H_2 and CO about several molecular gas peaks. These peaks are indicated in Figure 7 and summarized in Table 5. We normalize each profile by its peak value, so Figure 11 contains no information about the relative amplitude of the two distributions, i.e., X_{CO}. Instead, Figure 11 shows the relative structure in the two maps. For four of the six peaks, H_2 is more extended than CO; around one peak CO is more extended than H_2; and around one peak, the N83/N84 region in the east, CO and H_2 have similar structure.

We stack the normalized profiles and measure the half-width at half-maximum (HWHM) for the average H_2 and CO profiles. The stacked H_2 has HWHM ~ 41 pc, while the stacked CO has HWHM ~ 30 pc. Integrating the average H_2 profile and the average CO profile, we find $\int \Sigma_{H_2} / \int \Sigma_{CO} = 1.3$. Thus, along an average line of sight toward a molecular peak, $\sim$30% of the H_2 lies outside of the region with CO emission, a number we used to compute the "common volume" X_{CO} estimate above.

Figure 12 shows another view of the relative distribution of H_2 and CO. We plot regions with $\Sigma_{H_2} > 60\,M_\odot$ pc^{-2} in gray and indicate the extent of significant CO emission (3 $\sigma = 0.3$ K km s^{-1}) with black contours. These two thresholds are matched for $X_{CO} = (13 \pm 1) \times 10^{21}$ cm^{-2} (K km s^{-1})$^{-1}$, our integrated conversion factor. Note that this is $\sim$2 times higher than our estimate of X_{CO} over the shared volume. Therefore, the gray area in Figure 12 shows a very conservative estimate of where we would expect to find CO emission based on our FIR-derived Σ_{H_2}. Despite this conservative cut, toward regions of active star formation, at the north and south of the bar and in the eastern N83 region, H_2 extends beyond the CO. In these regions, the dust is warm and Figures 12 and 8 give us confidence that our FIR-based H_2 map traces Σ_{H_2} better than CO.

Thus, we present three measurements that suggest the H_2 to be more extended than the CO: (1) the profiles shown in Figure 11; (2) the large extent of CO relative to H_2 at a common, conservative threshold in Figure 12; and (3) most compellingly, the measurement of different values of X_{CO} averaging over low- and high-I_{CO} regions: where $I_{CO} > 0.3$ K km s^{-1} we find $X_{CO} = (9 \pm 1) \times 10^{21}$ cm^{-2} (K km s^{-1})$^{-1}$, and where $I_{CO} < 0.3$ K km s^{-1} we find $X_{CO} = (18 \pm 2) \times 10^{21}$ cm^{-2} (K km s^{-1})$^{-1}$. None of these measurements depend critically on the amplitude of the H_2 map, i.e., M_{H_2}, or the sensitivity of the CO map, but only on the relative structure of the H_2 and CO maps. We interpret this increase in H_2 relative to CO toward the outer parts of SMC clouds as evidence of the selective photodissociation of CO in these regions (Maloney & Black 1988).

Away from the star-forming regions, there is more CO relative to FIR-derived H_2. Several small CO clouds—in the wing, the central bar, and outside the northern and southern star-forming regions—may be good candidates to harbor populations of cold dust. In these regions, we still find significant H_2 emission: 90% of lines of sight with $I_{CO} > 0.3$ K km s^{-1} also have $\Sigma_{H_2} > 20\,M_\odot$ pc^{-2} (3 σ), and the remainder all have Σ_{H_2} at slightly lower significance. However, toward these regions we may underestimate the total Σ_{H_2} because there is a population of cold dust that is incompletely traced by our FIR maps.

How much molecular gas is represented by these quiescent clouds? The region with $\Sigma_{H_2} > 60\,M_\odot$ pc^{-2} contains both 70% of the significant CO emission and 70% of the significant H_2 surface densities. While the FIR-based Σ_{H_2} may fail in these regions, they will be subject to less intense radiation fields and should therefore suffer less selective photodissociation of CO. Therefore, based on the fraction of the total CO luminosity coming from such clouds, we estimate the fraction of the SMC molecular phase in cold, quiescent clouds to be $\sim$30%.

4.2.3. *Surface Density and Extinction*

If photoionization by far-UV photons regulates the structure of molecular clouds, then GMCs in low-metallicity systems may be expected to have higher surface densities than Milky Way GMCs in order to achieve the same mean extinction as their Galactic counterparts (average $A_V \approx 4$–8 over a Milky Way GMC; McKee 1989; Solomon et al. 1987). Pak et al. (1998) estimated $N(\mathrm{H}) \gtrsim 10^{23}$ cm^{-2} ($\Sigma_{\mathrm{H}} \gtrsim 800\,M_\odot$ pc^{-2}) toward SMC star-forming

regions. Using our dust and gas maps, we calculate the mean surface density and extinction toward the molecular peaks in the SMC.

We find surface densities similar to those of spiral galaxy GMCs rather than the values of $\gtrsim$1000 $M_\odot$ pc^{-2} expected from McKee (1989) and Pak et al. (1998). The molecular gas peaks indicated in Figure 7 have surface densities $\Sigma_{H_2} = 90$–310 with a mean $\Sigma_{H_2} = 180 \pm 30\ M_\odot$ pc^{-2}. This is similar to the mean for Milky Way GMCs, $\Sigma_{H_2} \approx 170\ M_\odot$ pc^{-2} (Solomon et al. 1987). If CO-dark H_2 makes up 10%–50% of the molecular gas in the Milky Way (Grenier et al. 2005), SMC clouds may even have Σ_{H_2} slightly lower than Galactic clouds. Along the same lines of sight, the H I surface density varies from $\Sigma_{H\,I} = 35$ to 105 $M_\odot$ pc^{-2} with a mean of $\Sigma_{H\,I} \approx 70 \pm 10\ M_\odot$ pc^{-2}. Over the entire region with 3 σ CO emission, a reasonable estimate of the star-forming area, we find a mean $\Sigma_{H_2} = 90 \pm 10\ M_\odot$ pc^{-2} and a mean $\Sigma_{H\,I} = 65 \pm 2\ M_\odot$ pc^{-2}.

Nearly Galactic surface densities imply that the mean extinction through SMC GMCs is much lower than in Galactic GMCs. Bouchet et al. (1985) found $R_V = A_V/E(B-V) = 2.7 \pm 0.2$ for the SMC. Using this value and $N_H/E(B-V) = 5.8 \times 10^{21}$ cm^{-2} mag^{-1} (Bohlin et al. 1978), scaled down by the D/H relative to Galactic (taken here to be $\approx$0.01), we calculate A_V:

$$A_V \approx \frac{N(\mathrm{H\ I}) + 2N(\mathrm{H_2})}{2.1 \times 10^{21}\ \mathrm{cm^{-2}}} \frac{\mathrm{D/H_{SMC}}}{\mathrm{D/H_{MW}}}. \quad (5)$$

We measure $(\mathrm{D/H_{SMC}})/(\mathrm{D/H_{MW}})$ to be $\approx$7 (§ 3.2). Using equation (5), we find $A_V \approx 1.8 \pm 0.6$ mag toward the molecular peaks and $A_V \approx 1.1 \pm 0.5$ mag over the whole region with CO emission. Applying the method of Schlegel et al. (1998) to our dust map yields consistent extinctions, $A_V \approx 1.6 \pm 0.3$ toward the peaks and $A_V \approx 1.0 \pm 0.4$ over all CO emission.

Our H_2 map has 46 pc resolution, close to the average diameter of a Milky Way GMC (Solomon et al. 1987). If the star-forming parts of SMC GMCs have the same diameters as Milky Way clouds, then our data are not consistent with the high surface densities predicted by McKee (1989) for low-metallicity GMCs. However, the region of CO emission, rather than the more extended H_2 region, may be the relevant comparison for the McKee (1989) prediction. We only expect star formation to occur within the CO-emitting region, and the $\bar{A}_V = 4$–8 calculated by McKee (1989) is for GMCs defined by CO emission. In this case, resolution effects ("beam dilution") may cause us to underestimate the surface density associated with the CO peaks. If the radius of a typical SMC GMC is $\sim$15 pc, for example, then the associated surface density of H_2 may be $\sim$1600 $M_\odot$ pc^{-2}, consistent with the McKee & Zweibel (1992) prediction. Many structures in the N. Mizuno et al. (2007, in preparation) CO map are unresolved or only marginally resolved, and other studies have indicated that CO clouds in both LMC and SMC may be smaller than in the Milky Way, with CO confined to small regions and little or no diffuse component (e.g., Lequeux et al. 1994; Rubio 1999; Mizuno et al. 2001).

Thus, we find evidence for differences between SMC and Milky Way GMCs but cannot distinguish the sense of them because of limited resolution. SMC GMCs either have lower average extinction through the clouds or are substantially ($\sim$3 times) smaller on average than Milky Way GMCs. A second high-resolution band is needed to test which of these conclusions holds by measuring the surface densities of SMC GMCs at a resolution of $\approx$10 pc (that of the MIPS 160 μm map).

4.2.4. *Pressure and Molecular-to-Atomic Gas Ratio*

In spiral galaxies there is a good correlation between the ratio of molecular gas mass to atomic gas mass and the hydrostatic midplane pressure (Blitz & Rosolowsky 2004). Dust is integral to H_2 formation and may impede H_2 destruction (although self-shielding of H_2 may also have this effect). Therefore, we expect that, given the low DGR in the SMC, the ratio of molecular gas to atomic gas for a given pressure (gas density) will be lower in the SMC than in spiral galaxies.

Blitz & Rosolowsky (2004) derive that the hydrostatic midplane pressure for a thin disk of gas in a larger disk of stars is

$$P_h = 0.84 (G\Sigma_*)^{0.5} \Sigma_g \frac{v_g}{(h_*)^{0.5}}, \quad (6)$$

where Σ_g is the total surface density of the gas, Σ_* is the surface density of stars, v_g is the velocity dispersion of the gas, and h_* is the scale height of the stellar disk. The applicability of this formula in the SMC is questionable: the three-dimensional distribution of the stellar potential is likely not well described as a disk. Indeed, Crowl et al. (2001) find a 1 σ dispersion of 6–12 kpc along the line of sight through the SMC. They suggest that the galaxy may be a triaxial spheroid with a 1:2:4 ratio of sizes along the right ascension, declination, and line-of-sight directions. Also, although there is usually only a single molecular complex along a given line of sight, there are often several H I components. Even if equation (6) applies, the inclination, stellar scale height, and the mass-to-light ratio of the stellar and gas disks are not known to better than a factor of 2.

Emphasizing the approximate nature of the calculation, we derive the pressure and the ratio of molecular to atomic gas at $\sim$0.7° resolution ($\sim$750 pc). The mean velocity dispersion of H I along the line of sight is $v_g \approx 20$ km s^{-1} (Stanimirović et al. 1999). We adopt $h_* = 6$ kpc (the low end of the Crowl et al. [2001] range) and no inclination. We use the DIRBE K-band map and a mass-to-light ratio $M/L_K = 0.5\ M_\odot\ L_{K,\odot}^{-1}$ (e.g., Simon et al. 2005) to calculate Σ_* and the FIR-based H_2 map combined with the H I map to calculate the gas surface density and the ratio of molecular to atomic gas.

Figure 13 shows f_{mol} as a function of P_h for the SMC and a sample of spiral galaxies studied by Blitz & Rosolowsky (2006) with similar spatial resolution. Most lines of sight for the SMC have $P_h/k_B = 10^4$–10^5 K cm^{-3}, with almost half of the data in the bin centered on $P_h/k_B = 2.4 \times 10^4$ K cm^{-3}. In this bin, the best-fit Blitz & Rosolowsky (2006) relation predicts $f_{mol} \approx 0.6$ for large spiral galaxies. For reference, this P_h and f_{mol} are similar to those found at the solar circle in the Milky Way, a region that is dominated by H I by about 2:1. In the SMC we measure $f_{mol} = 0.2$ in the bin centered on $P_h/k_B = 2.4 \times 10^4$ K cm^{-3}, a factor of 3 lower than the prediction/Milky Way value. Over the whole SMC, we find f_{mol} a factor of 2–3 lower than predicted.

Thus, Figure 13 suggests that the low ratio of H_2 to H I in the SMC is due to a combination of low gas densities and environmental effects. Because the median P_h in the SMC is lower than in the inner disks of spiral galaxies, f_{mol} is low. However, f_{mol} is lower than found in spiral galaxies by an additional factor of 2–3. This may be the result of the low DGR. We suggest the following explanation: Because the formation rate of H_2 is limited by the rate at which H atoms stick to the surface of dust grains (Hollenbach et al. 1971), H_2 will form more slowly in the dust-poor SMC. This lower formation rate means that given the same conditions (density, shielding from dissociating radiation), the equilibrium H_2/H I ratio should be lower for a low DGR galaxy. Alternatively, SMC clouds may be out of equilibrium: for a low DGR, an H I cloud will take longer to convert to H_2, even under conditions where an overwhelmingly molecular cloud is the equilibrium state (Bell et al. 2006). If the timescale to reach

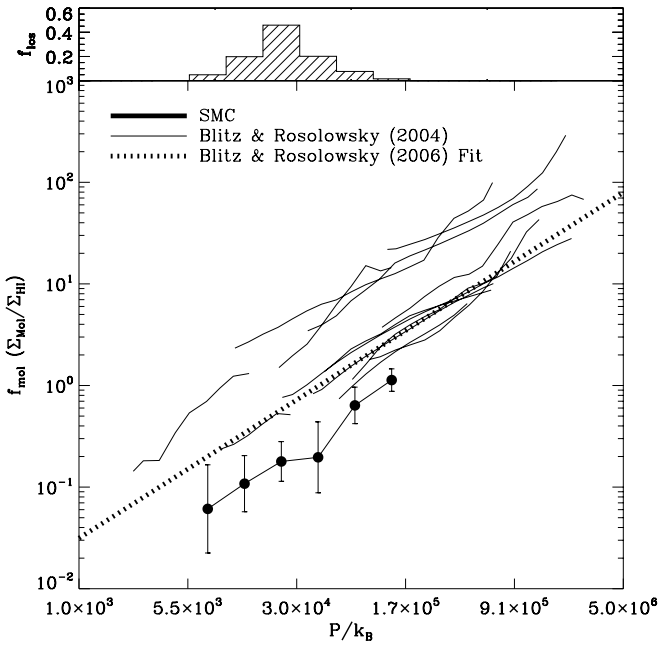

FIG. 13.—Molecular-to-atomic gas ratio, $f_{\rm mol}$, as a function of hydrostatic midplane pressure, conducted at 0.7° resolution. We use the formula of Blitz & Rosolowsky (2004) with $\sigma_v = 20$ km s^{-1} and $h_* = 6$ kpc and also plot data for spiral galaxies measured at comparable spatial resolution (Blitz & Rosolowsky 2006). The histogram above the plot shows the fraction of lines of sight in each pressure bin for the SMC. The low H_2–to–H I ratio in the SMC is a result of the relatively low values of P_h and an additional factor of ~3 deficit that may be the result of a low DGR.

equilibrium is long compared to the cloud lifetime, then these clouds may never reach chemical equilibrium. In this case, we may expect to find a lower ratio of molecular gas to atomic gas in low-metallicity galaxies like the SMC.

5. CONCLUSIONS

We present new FIR maps of the SMC at 24, 70, and 160 μm obtained by *Spitzer* as part of the S^{3}MC survey (Bolatto et al. 2007). These maps cover the bar and the wing regions with 6″, 18″, and 40″ resolution at 24, 70, and 160 μm, respectively (1.8, 5.4, and 12 pc). Combining these maps with data from the literature, we draw the following conclusions:

1. We find a total $M_{\rm dust} = 3 \times 10^5\ M_\odot$, which is systematically uncertain by a factor of 2–3 because of degeneracies in how to model the dust. Strong upper and lower limits to the dust mass in the SMC are $\sim 2 \times 10^4$ and $10^6\ M_\odot$, respectively.

2. If the long-wavelength part of the SMC SED comes from a population of very cold dust, then $M_{\rm dust}$ is a lower limit. However, based on the lone GMC with published, resolved millimeter observations, it seems unlikely that GMCs harbor the requisite amount of cold dust to account for the long-wavelength emission. There are plausible alternative explanations: an abundance of hot VSGs or that the emissivity of SMC grains at long wavelengths differs from the Galactic value. The latter explanation is simple and consistent with the data.

3. The dust-to-hydrogen ratio, D/H, over the whole region studied is $\log_{10}({\rm D/H}) = -2.86$, or 1:700, including H_2, implying a total $\log_{10}{\rm DGR} \approx -3.0$. This is about $Z_{\rm SMC}/Z_{\rm MW}$ times the Milky Way DGR and is consistent with Bouchet et al. (1985) and Wilke et al. (2004).

4. The dust–to–H I ratio, D/H I, is a function of position in the SMC. In the wing and the bar, we find mean $\log_{10}({\rm D/H\ I_{wing}}) = -2.94 \pm 0.02$ and $\log_{10}({\rm D/H\ I_{bar}}) = -2.71 \pm 0.01$. D/H I near regions with CO emission is higher still: $\log_{10}({\rm D/H\ I_{CO}}) = -2.54 \pm 0.02$. Some of this high value may be due to enhancements in the opacity and abundance of dust in molecular clouds, e.g., due to growth of icy mantles. However, we argue that most of the D/H I enhancement near CO emission is best explained by the presence of molecular hydrogen.

5. Following a method outlined by Israel (1997b) and Dame et al. (2001), we derived a map of Σ_{H_2} in the SMC. To derive this map, we calibrate D/H locally using a set of reference regions shown in Figure 7 and apply equations (3) and (4). We find $M_{H_2} = 3.2 \times 10^7\ M_\odot$ of H_2 in the SMC, equal to ~10% of the H I mass. This is lower than the ratio of molecular to atomic gas found in the inner parts of spiral galaxies, but similar to that found in dwarf galaxies and the outer parts of spiral galaxies (Young & Scoville 1991; Israel 1997a; Leroy et al. 2005; see also Fig. 13).

6. The derived CO-to-H_2 conversion factor over the entire SMC is $(13 \pm 1) \times 10^{21}$ cm^{-2} (K km s^{-1})$^{-1}$, similar to that obtained by Israel (1997b). Toward molecular peaks, correcting for H_2 beyond the CO along the line of sight, we find a conversion factor of $(6 \pm 1) \times 10^{21}$ cm^{-2} (K km s^{-1})$^{-1}$. This represents our best value of $X_{\rm CO}$ for comparison with virial mass measures. It is still 2–4 times larger than virial $X_{\rm CO}$ measurements for SMC GMCs.

7. SMC GMCs appear to be gravitationally bound. We measure M_{H_2} to be larger than $M_{\rm vir}$, surface densities similar to those of Milky Way GMCs, and a mean midplane pressure similar to that at the solar circle (albeit with a large systematic uncertainty).

8. We find evidence for the selective photodissociation of CO. About the molecular peaks, H_2 is more extended than CO by about 30%. Averaging over low-CO ($I_{\rm CO} < 0.3$ K km s^{-1}) and high-CO ($I_{\rm CO} > 0.3$ K km s^{-1}) regions, we find that the low-CO regions have twice as much H_2 per CO as the high-CO regions. We average over a large region to make these measurements, so this is not a sensitivity effect. Regions of high H_2-to-CO occur near intense radiation fields surrounding bright CO clouds, consistent with the scenario in which the outer parts of SMC clouds see their CO destroyed by UV photons while H_2 survives due to self-shielding (Maloney & Black 1988).

9. Several clouds away from massive star formation show more CO relative to FIR than average, making them good candidates to harbor populations of cold dust. One of these clouds, SMC B1 No. 1 (Rubio et al. 2004), shows a greater submillimeter-to-FIR ratio than the SMC as a whole. These clouds represent ~30% of the total CO luminosity.

10. GMCs in the SMC are either translucent or very small. SMC molecular peaks have H_2 surface densities similar to Milky Way GMCs, $\Sigma_{H_2} \approx 100$–$200\ M_\odot$ pc^{-2}, and extinctions of $A_V \approx 1$–2 mag. This is lower than the $A_V = 4$–8 mag found in Milky Way clouds (McKee 1989). Either photoionization by far-UV photons does not regulate the structure of SMC GMCs and they indeed have lower average extinctions, or the star-forming parts of SMC GMCs are a factor of ~3 smaller than our 46 pc beam.

11. The low H_2–to–H I ratio in the SMC results from a combination of low gas densities and metallicity effects. The SMC has a lower ratio of molecular to atomic gas by a factor of 2–3 than expected based on its hydrostatic pressure (and Blitz & Rosolowsky 2006), but also a median pressure a factor of ~3 lower than large galaxies. The median P_h is comparable to that at the solar circle, although very uncertain.

This work is based on observations made with the *Spitzer Space Telescope*, which is operated by the Jet Propulsion Laboratory,

California Institute of Technology, under a contract with NASA. This research was partially supported by NSF grant AST 02-28963. Partial support for this work was also provided by NASA through an award issued by JPL/Caltech (NASA-JPL Spitzer grant 1264151 awarded to Cycle 1 project 3316). We made use of the NASA/IPAC Extragalactic Database (NED), which is operated by the Jet Propulsion Laboratory, California Institute of Technology, under contract with the National Aeronautics and Space Administration; and NASA's Astrophysics Data System (ADS). This research has made use of the NASA/IPAC Infrared Science Archive, which is operated by the Jet Propulsion Laboratory, California Institute of Technology, under contract with the National Aeronautics and Space Administration. We wish to especially thank L. Blitz, C. McKee, and J. Graham, who all gave critical readings of this work while it was being prepared as part of A. L.'s thesis, and F. Boulanger, who kindly provided suggestions on reading a draft. We also thank the anonymous referee for suggestions that improved this work.

APPENDIX A

CALIBRATING THE MIPS 160 μm MAP

Figure 6 and Table 3 show that there is good photometric consistency among our data. Fluxes at the same wavelength agree within the uncertainties, and the data are consistent with DIRBE, which represents the best measurements of absolute sky brightness at FIR wavelengths. The exception to the general good agreement is that the 160 μm contains more flux than we expect based on comparison with the DIRBE data at 140 and 240 μm and the *ISO* 170 μm map. In this section we describe how we use the DIRBE data to calibrate the MIPS 160 μm map. The calibrated 160 μm map is used for all of the results in this paper, including Figure 6 and Table 3. Our approach to calibrating the 160 μm map is as follows:

1. We adopt DIRBE as our absolute calibration.
2. From the DIRBE bands at 140 and 240 μm we estimate the intensity at 160 μm by interpolation. We adopt $\beta = 2$ and calculate a temperature from the ratio of the 140 μm to 240 μm bands. The method of interpolation makes little ($\lesssim$10%) difference because the 140 μm DIRBE band is close to the 160 μm MIPS band.
3. The foreground-subtracted DIRBE data (see § 2) are our estimate of the 160 μm intensity from the SMC along each line of sight. We add our best estimate of the MIPS 160 μm foreground (from zodiacal light, Galactic cirrus, and the CIB) to this value. This is our best estimate of the intensity that MIPS *should* measure.
4. We make the decision to model the difference between MIPS and DIRBE using one parameter: the best-fit gain. This is the ratio of the intensities measured by MIPS to those that it should measure as estimated from DIRBE, $I_{\mathrm{DIRBE},160\ \mu\mathrm{m}}/I_{\mathrm{MIPS},160\ \mu\mathrm{m}}$.
5. We derive the best value for the gain by taking the average ratio of predicted to measured intensity over the MIPS map. We perform the comparison at the DIRBE resolution, 0.7°. We use DIRBE to fill in empty parts of the MIPS map, but we only consider lines of sight for which at least 75% of the data within the beam come from MIPS. This average ratio is 0.8, so that $I_{\mathrm{DIRBE},160\ \mu\mathrm{m}} = 0.8 I_{\mathrm{MIPS},160\ \mu\mathrm{m}}$; the median and integrated ratios are within a few percent of this value.
6. We apply this factor to the MIPS data before foreground subtraction and proceed as described above. Scaling by 0.8 before foreground subtraction lowers the flux of the MIPS map by ~5000 Jy.

The [C II] 158 μm line lies in the MIPS 160 μm bandpass but not the nearby DIRBE bands. However, we show below that reasonable estimates of the contribution by this interstellar cooling line are too low to explain the excess flux in the MIPS map. Instead, the difference may be a result of the mapping method or simply an offset between the MIPS and DIRBE calibrations for the run over which the SMC data were taken. Throughout this paper we adopt the DIRBE absolute flux calibration and use the rescaled MIPS map. We mention the effect that excess emission at 160 μm would have on our results in the discussion of uncertainties.

Figure 14 shows the calibrated MIPS 160 μm data convolved to 0.7° and 1.5′ and plotted against data from DIRBE and *ISO*. We bin the data by intensity and plot the mean and rms scatter for each bin. Arbitrarily normalized histograms below each plot show the relative distribution of intensities for *ISO* and DIRBE and so give an idea of the importance for each point. The agreement between MIPS and the other data is good, particularly over the range of common intensities (high values in the histogram). The calibration could be improved by adding additional parameters (e.g., an intercept or quadratic term), but this runs the risk of skewing our results by overprocessing the data. Figure 14 may serve as a guide to the reader of the uncertainty in the calibration.

In the remainder of this appendix, we show that the discrepancy between MIPS and DIRBE is too large to be accounted for by the [C II] 158 μm fine-structure line or the known MIPS light leak.

A1. IS THE EXCESS DUE TO [C II] EMISSION?

The [C II] 158 μm line lies in the MIPS 160 μm bandpass. Does contamination by this important interstellar cooling line explain the discrepancy between the MIPS and DIRBE data? No extensive maps of the [C II] line in the SMC are available, so we estimate the [C II] contamination of the 160 μm map in two ways: by extrapolating from measurements of [C II] in a few star-forming regions, and by using the [C II]–to–FIR and [C II]–to–CO ratios measured in other galaxies.

Israel & Maloney (1993) and Bolatto et al. (2000a) both measured the [C II] line toward several star-forming regions. Using the Kuiper Airborne Observatory (KAO), Israel & Maloney (1993) found an integrated [C II] line flux across five of the brightest star-forming regions that corresponds to ~50 Jy averaged across the 4×10^{11} Hz MIPS bandpass (F. Israel 2006, private communication). Although the KAO measurements cover only a small portion of the SMC, they do include the brightest star-forming regions that account for $\approx$10% of the FIR emission. If [C II] emission is directly proportional to FIR emission across the SMC (rather than preferentially concentrated in PDR/star-forming regions), then [C II] emission from the SMC totals ~500 Jy.

Stacey et al. (1991) found that the [C II] emission accounts for 0.1%–1% of the FIR luminosity from a star-forming galaxy. The integrated FIR flux from the SMC based on *IRAS* is $\sim 4 \times 10^{-10}$ W m^{-2}, so we expect $\sim 10^2$–10^3 Jy from the [C II] line in the SMC based

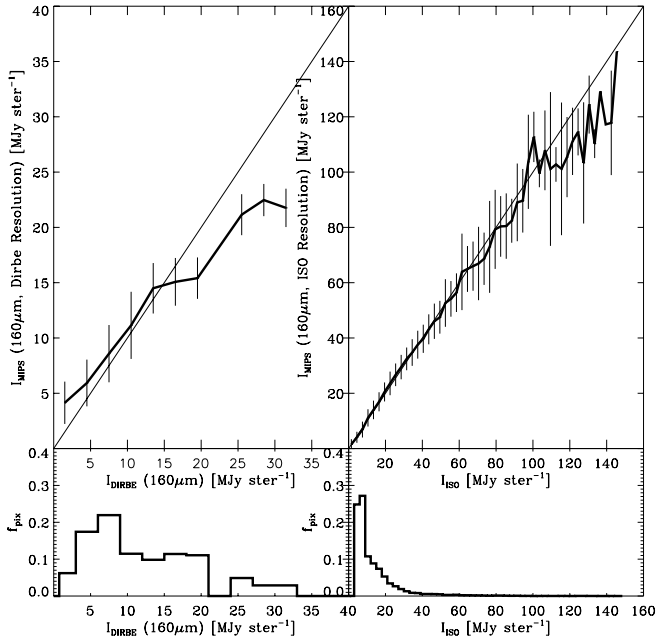

FIG. 14.— MIPS 160 μm flux after correction (scaling by 0.8) and convolution to the DIRBE (*left*) and *ISO* (*right*) resolution plotted as a function of DIRBE interpolated to 160 μm from nearby wave bands (*left*) and *ISO* (*right*). We bin the data by intensity and then plot the mean and rms scatter in each bin. The agreement with *ISO* is good, but at high intensities the MIPS data are 20%–30% lower than the DIRBE data, probably because of saturation effects. Normalized histograms show the distribution of intensities for both data sets.

on the FIR emission. Mochizuki et al. (1998) and Madden et al. (1997) report ratios between the [C II] and CO $J = 1 \rightarrow 0$ line fluxes of 10^4–10^5 for some actively star-forming dwarf galaxies. Mizuno et al. (2001) find the integrated CO intensity of the SMC to be $\sim 10^5$ K km s^{-1} pc^2, implying a flux from the CO line of 3×10^{-17} W m^{-2}. If the SMC has a ratio of [C II] to CO emission consistent with the other dwarfs, this implies a [C II] luminosity of 10^2–10^3 Jy, consistent with the estimate from the FIR.

Thus, several lines of argument suggest that the [C II] line contributes 10^2–10^3 Jy to the MIPS 160 μm band. The most likely scenario is that a few hundred janskys of emission of total luminosity in the MIPS bandpass can be attributed to the [C II] line. This is significantly less than the $\sim$5000 Jy needed to explain the discrepancy between the MIPS 160 μm band and the emission in nearby DIRBE bands.

A2. IS THE EXCESS DUE TO THE MIPS LIGHT LEAK?

The known light leak into MIPS from the near-IR cannot be the source of the flux discrepancy and does not represent a concern. According to the MIPS Data Handbook, data with a 160 μm/2 μm flux density ratio greater than 0.004 will be uncorrupted by the light leak. Estimated from the DIRBE data, the median ratio of 160 μm flux density to 2 μm flux density along lines of sight toward the SMC is 75 and is never less than 35.

APPENDIX B

PRODUCING THE DUST MAP

In this section we describe how we use the *IRAS* 100 μm and MIPS 160 μm data to construct a map of the dust mass surface density, $\Sigma_{\rm dust}$, in the SMC. We then give brief descriptions of the sources of uncertainty that may affect this map, summarized in Table 7.

B1. METHOD

Deriving the dust mass surface density $\Sigma_{\rm dust}$ follows this basic method:

1. Estimate the dust temperature, T, or distribution of temperatures along the line of sight.
2. Adopt an emissivity for the dust. This consists of a mass absorption coefficient, κ_ν, and a power-law wavelength dependence, $\kappa_\nu \propto \lambda^{-\beta}$, with an index β.
3. Convert the amplitude of the FIR emission into a dust mass surface density. For a single dust population,

$$\Sigma_{\rm dust}\left(\text{g cm}^{-2}\right) = \frac{I_\nu(\text{MJy sr}^{-1})}{\kappa_\nu(\text{cm}^2\ \text{g}^{-1}) B_\nu(T)(\text{MJy sr}^{-1})}, \tag{B1}$$

where $B_\nu(T)$ is the specific intensity of a blackbody with temperature T at a frequency ν and I_ν is the intensity of measured FIR emission at the same frequency.

TABLE 7
Uncertainties in the Dust Map

Description	Sense	Magnitude
Data:		
Statistical[a]	±	≲10%
Foreground	±	20%
Calibration	+	80%
Saturation	+	≲10%
Choice of model:		
Power law vs. single population	Divide	3
Choice of bands[b]	...	50%
$U_{\rm min}$[c]	Multiply	2+
κ_{250}	Multiply	2
β	...	20%

[a] Per line of sight. Negligible over the whole SMC.
[b] If the 60 and 100 μm bands are used instead of the 100 and 160 μm bands.
[c] In the limit, this is the same as the cold dust concern.

Our data have limited spatial resolution ($\sim$75 pc at 100 μm), and each line of sight through the SMC is probably several kiloparsecs long with more than one H I velocity component. As a result, we expected several populations of dust to contribute along each line of sight. Therefore, we treat the SMC using models presented by Dale et al. (2001) and refined in Dale & Helou (2002). These models consider dust that is illuminated by a distribution of radiation fields, U, ranging from 0.3 to 10^5 times the local intensity. They use an updated version of the description of interstellar dust by Désert et al. (1990). The free parameters in the model are the power-law index, α, of dust mass as a function of illuminating radiation field and the total dust mass, $M_{\rm dust}$, proportional to the amplitude of the spectrum. These parameters, α and $M_{\rm dust}$, are related by

$$dM_{\rm dust} \propto U^{-\alpha}\, dU, \tag{B2}$$

so that the lower the value of α, the hotter the dust, on average.

We derive $\Sigma_{\rm dust}$ for each line of sight by using the observed 100 μm–to–160 μm color to pick the best Dale & Helou (2002) model, identified by its power-law index α. From the amplitude of the FIR emission and the model SED associated with that α we compute the dust mass along the line of sight. Dale et al. (2001) emphasize that the models are well distinguished by the I_{60}/I_{100} color alone. The 100 μm–to–160 μm color appears to do almost as good a job while avoiding the 24–70 μm bands. These bands introduce additional free parameters because they contain substantial contributions from PAHs and VSGs (Désert et al. 1990), the relative mix of which (i.e., the exact dust size distribution) is not well known in the SMC.

B2. UNCERTAINTIES

Statistical.—The statistical uncertainty associated with the map is modest. We repeatedly add noise with a magnitude from Table 2 to the data and estimate the 1 σ uncertainty in $\Sigma_{\rm dust}$ to be 8% at 2.6′ resolution and 4% at 4′ resolution. The uncertainty in $M_{\rm dust}$ is thus dominated by the choice of method, model, and systematic uncertainties in the data.

Foreground subtraction.—The uncertainty associated with the foreground subtraction can have a sizeable impact, particularly in the diffuse (low intensity) wing. We test the effect of errors in the foreground subtraction by adding and then subtracting 1 MJy sr^{-1} to the 100 μm map and then the 160 μm map. This offset results in a ±20% change in the total dust mass over the SMC. In regions of low intensity an offset of 1 MJy sr^{-1} in one band may affect the dust surface density by up to 50%.

Calibration and saturation.—If the MIPS calibration (rather than DIRBE) is correct, then our MIPS 160 μm map should be scaled by $\sim$1.25. This results in a dust content $\sim$80% higher than we find. The possible saturation concerns for regions with $I_{160} > 50$ MJy sr^{-1} only have a small impact (<10%) on the derived dust mass.

Power law versus single population.—The dust mass derived using the Dale & Helou (2002) models is a factor of $\sim$3 higher than one would derive using a single $\beta = 2$ population and the 100 and 160 μm bands to model each line of sight. Figure 15 shows this difference by plotting the key quantity, $\Sigma_{\rm dust}$ per unit 160 μm emission, as a function of the 100 μm–to–160 μm color. Figure 15 also shows the relative distribution of sight lines with each color in the SMC and illustrates several other systematic effects discussed in this section.

$U_{\rm min}$ and $U_{\rm max}$.—The upper and lower limits to the radiation field distribution, $U_{\rm min}$ and $U_{\rm max}$, may affect the derived dust mass. Dale et al. (2001) and Dale & Helou (2002) constructed their models to match the integrated SEDs of a sample of several dozen star-forming galaxies, so $U_{\rm min} = 0.3$ and $U_{\rm max} = 10^5$ times the local value are motivated by observations. However, we test the effects of varying $U_{\rm min}$ and $U_{\rm max}$ on a simple model that includes only BGs with $\kappa_{250} = 15$ cm^2 g^{-1}. The value of $U_{\rm min}$ strongly affects dust mass, but $U_{\rm min}$ cannot be much higher than $\approx$0.5 or the models will not be able to reproduce the lowest I_{100}/I_{160} ratios seen in the SMC. Varying $U_{\rm max}$ has minimal effect over the range of colors observed in the SMC. Dust illuminated by $U = 0.3$ has $T \approx 14.5$ K, so the uncertainty regarding $U_{\rm min}$ is a restatement of the potential population of very cold dust. Dust with $T \lesssim 15$ K has $\log_{10}(I_{100}/I_{160}) \lesssim -0.5$. Figure 15 shows that there are very few lines of sight in the SMC with $\log_{10}(I_{100}/I_{160}) \lesssim -0.3$, let alone -0.5.

Choice of bands (*inclusion of VSGs*).—The Dale & Helou (2002) models account for the contribution from VSGs, albeit with a Galactic mix of grain types. Therefore, the choice to omit the 60 and 70 μm bands has a relatively small impact. Using the 100 and 160 μm data yields a mass 50% higher than the 60 and 100 μm data, presumably because the SMC has more VSGs than the Milky Way

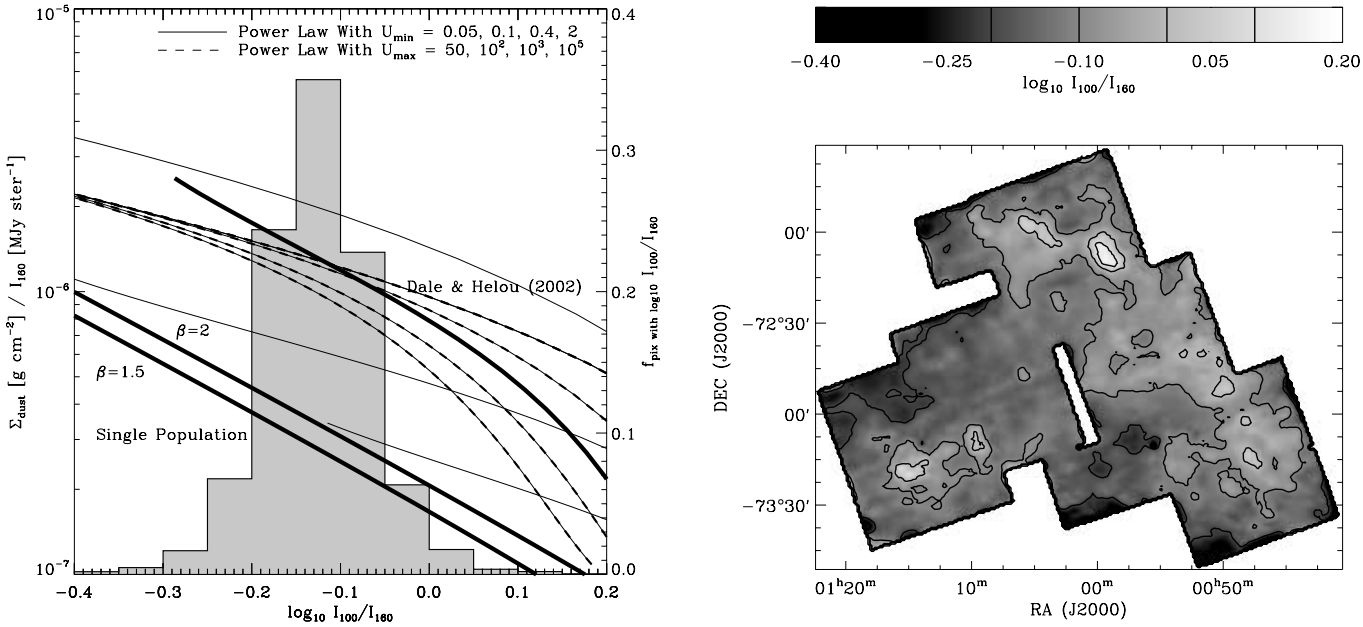

FIG. 15.—A look at the methodology used to create our dust map. *Left*: Normalized histogram of the 100 μm–to–160 μm color for the SMC along with the dust mass surface density per unit 160 μm intensity, Σ_{dust}/I_{160}, as a function of FIR color, $\log_{10}(I_{100}/I_{160})$, for several simplified models. The three thick lines show the relationship for a single population of dust with $\beta = 1.5$, one with $\beta = 2$, and the power-law models by Dale & Helou (2002). The thin lines show the same relationship for simple power-law models with the minimum (*solid*) and maximum (*dashed*) radiation field varied. (We vary the maximum radiation field about $U_{min} = 0.1$ because it is the value for which our simple calculations best match the Dale & Helou 2002 models.) These lines show the impact of the assumptions that go into the Dale & Helou (2002) model. The maximum radiation field has very little impact, but the minimum radiation field affects the conversion between FIR intensity and dust mass surface density. *Right*: Map of the FIR color, $\log_{10}(I_{100}/I_{160})$, in the SMC. The star-forming regions have high 100 μm–to–160 μm ratios and are easily identified from the map.

mix adopted for the model. For the case of a single dust population it is critical to account for emission from VSGs if shorter wavelengths are included; failing to do so may result in estimates of dust masses an order of magnitude too low (this explains a factor of ~5 out of the difference between our results and those of Schwering 1988; Stanimirović et al. 2000; the choice of a power law as opposed to a single model explains the balance).

Mass absorption coefficient (κ_ν).—Alton et al. (2004) synthesize determinations of the emissivity from comparisons of optical and submillimeter/FIR emission along the same line of sight. They show that determinations of κ_{250} span from ≈5 to 15 cm^2 g^{-1}, a substantial scatter. The Dale & Helou (2002) models use a modified version of the Désert et al. (1990) dust model. Therefore, the dust map in this paper adopts their value of $\kappa_{250} \approx 9.5$ cm^2 g^{-1} (Draine & Lee 1984), a widely used value close to the middle of the range of literature determinations. The dust surface densities we derive are uncertain by a factor of 2 due to the uncertainty in the mass absorption coefficient. All of these values are not equally likely, but the value of $\kappa_{250} \approx 5$ cm^2 g^{-1} (Li & Draine 2001) is also commonly used.

Emissivity dependence on wavelength (β).—At long wavelengths, the wavelength dependence of κ_ν is usually treated as a power law with an index β, so that $\kappa_\nu \propto \lambda^{-\beta}$. However, there is substantial evidence that β may vary with environment (Dupac et al. 2003; Alton et al. 2004). The models by Dale & Helou (2002) incorporate an empirical radiation field dependence for β calibrated using submillimeter data for the sample of galaxies used to develop the Dale et al. (2001) and Dale & Helou (2002) models. For this calibration $\beta = 2.5$, 2.1, and 1.3 for radiations fields 1, 10, and 1000 times the local value. For the values of α we find in the SMC, $\beta \approx 2$. This may be too high; $\beta = 1.5$ may be more appropriate (see § 3.3). Because the 100 and 160 μm bands are fairly close in wavelength, the impact of changing β by this amount is small; we would find M_{dust} to be ≈20% lower for $\beta = 1.5$ than $\beta = 2$. Although it has a small effect on M_{dust}, β is important to interpreting the submillimeter excess observed toward the SMC (Aguirre et al. 2003). Further, since β seems to be a function of environment, variations between diffuse and dense gas may systematically affect our H_2 map (see main text).

REFERENCES

Aguirre, J. E., et al. 2003, ApJ, 596, 273
Alton, P. B., Xilouris, E. M., Misiriotis, A., Dasyra, K. M., & Dumke, M. 2004, A&A, 425, 109
Bajaja, E., Arnal, E. M., Larrarte, J. J., Morras, R., Pöppel, W. G. L., & Kalberla, P. M. W. 2005, A&A, 440, 767
Bell, T. A., Roueff, E., Viti, S., & Williams, D., A. 2006, MNRAS, 371, 1865
Blitz, L., Fukui, Y., Kawamura, A., Leroy, A., Mizuno, N., & Rosolowksy, E. 2007, in Protostars and Planets V, ed. B. Reipurth, D. Jewitt, & K. Keil (Tucson: Univ. Arizona Press), 81
Blitz, L., & Rosolowsky, E. 2004, ApJ, 612, L29
———. 2006, ApJ, 650, 933
Bohlin, R. C., Savage, B. D., & Drake, J. F. 1978, ApJ, 224, 132
Bolatto, A. D., Jackson, J. M., Kraemer, K. E., & Zhang, X. 2000a, ApJ, 541, L17
Bolatto, A. D., Jackson, J. M., Wilson, C. D., & Moriarty-Schieven, G. 2000b, ApJ, 532, 909
Bolatto, A. D., Leroy, A., Israel, F. P., & Jackson, J. M. 2003, ApJ, 595, 167
Bolatto, A. D., et al. 2007, ApJ, 655, 212
Bot, C., Boulanger, F., Lagache, G., Cambrésy, L., & Egret, D. 2004, A&A, 423, 567
Bouchet, P., Lequeux, J., Maurice, E., Prevot, L., & Prevot-Burnichon, M. L. 1985, A&A, 149, 330
Boulanger, F., Abergel, A., Bernard, J.-P., Burton, W. B., Desert, F.-X., Hartmann, D., Lagache, G., & Puget, J.-L. 1996, A&A, 312, 256
Cambrésy, L., Boulanger, F., Lagache, G., & Stepnik, B. 2001, A&A, 375, 999
Crowl, H. H., Sarajedini, A., Piatti, A. E., Geisler, D., Bica, E., Clariá, J. J., & Santos, J. F. C., Jr. 2001, AJ, 122, 220
Dale, D. A., & Helou, G. 2002, ApJ, 576, 159
Dale, D. A., Helou, G., Contursi, A., Silbermann, N. A., & Kolhatkar, S. 2001, ApJ, 549, 215
Dame, T. M., Hartmann, D., & Thaddeus, P. 2001, ApJ, 547, 792
Désert, F.-X., Boulanger, F., & Puget, J. L. 1990, A&A, 237, 215
Draine, B. T., & Lee, H. M. 1984, ApJ, 285, 89

Dufour, R. J. 1984, in IAU Symp. 108, Structure and Evolution of the Magellanic Clouds, ed. S. van den Bergh & K. S. de Boer (Dordrecht: Reidel), 353
Dupac, X., et al. 2003, A&A, 404, L11
Dwek, E. 1998, ApJ, 501, 643
Galliano, F., Madden, S. C., Jones, A. P., Wilson, C. D., & Bernard, J.-P. 2005, A&A, 434, 867
Grenier, I. A., Casandjian, J.-M., & Terrier, R. 2005, Science, 307, 1292
Hauser, M. G., et al. 1998, ApJ, 508, 25
Heiles, C., Haffner, L. M., & Reynolds, R. J. 1999, in ASP Conf. Ser. 168, New Perspectives on the Interstellar Medium, ed. A. R. Taylor, T. L. Landecker, & G. Joncas (San Francisco: ASP), 211
Hilditch, R. W., Howarth, I. D., & Harries, T. J. 2005, MNRAS, 357, 304
Hollenbach, D. J., Werner, M. W., & Salpeter, E. E. 1971, ApJ, 163, 165
Israel, F. P. 1997a, A&A, 317, 65
———. 1997b, A&A, 328, 471
Israel, F. P., & Maloney, P. R. 1993, in New Aspects of Magellanic Cloud Research, ed. B. Baschek, G. Klare, & J. Lequeux (Berlin: Springer), 44
Issa, M. R., MacLaren, I., & Wolfendale, A. W. 1990, A&A, 236, 237
Keller, S. C., & Wood, P. R. 2006, ApJ, 642, 834
Kelsall, T., et al. 1998, ApJ, 508, 44
Lequeux, J., Le Bourlot, J., Des Forets, G. P., Roueff, E., Boulanger, F., & Rubio, M. 1994, A&A, 292, 371
Leroy, A., Bolatto, A. D., Simon, J. D., & Blitz, L. 2005, ApJ, 625, 763
Li, A., & Draine, B. T. 2001, ApJ, 554, 778
———. 2002, ApJ, 576, 762
Lisenfeld, U., & Ferrara, A. 1998, ApJ, 496, 145
Lisenfeld, U., Israel, F. P., Stil, J. M., & Sievers, A. 2002, A&A, 382, 860
Lisenfeld, U., Israel, F. P., Stil, J. M., Sievers, A., & Haas, M. 2005, in AIP Conf. Proc. 761, The Spectral Energy Distributions of Gas-rich Galaxies: Confronting Models with Data, ed. C. C. Popescu & R. J. Tuffs (New York: AIP), 239
Madden, S. C., Poglitsch, A., Geis, N., Stacey, G. J., & Townes, C. H. 1997, ApJ, 483, 200
Maloney, P., & Black, J. H. 1988, ApJ, 325, 389
Massey, P., Parker, J. W., & Garmany, C. D. 1989, AJ, 98, 1305
McKee, C. F. 1989, ApJ, 345, 782
McKee, C. F., & Zweibel, E. G. 1992, ApJ, 399, 551
Miville-Deschênes, M.-A., & Lagache, G. 2005, ApJS, 157, 302
Mizuno, N., Rubio, M., Mizuno, A., Yamaguchi, R., Onishi, T., & Fukui, Y. 2001, PASJ, 53, L45
Mochizuki, K., Onaka, T., & Nakagawa, T. 1998, in ASP Conf. Ser. 132, Star Formation with the *Infrared Space Observatory*, ed. J. Yun & R. Liseau (San Francisco: ASP), 386
Ossenkopf, V., & Henning, T. 1994, A&A, 291, 943
Pak, S., Jaffe, D. T., van Dishoeck, E. F., Johansson, L. E. B., & Booth, R. S. 1998, ApJ, 498, 735
Purcell, E. M. 1969, ApJ, 158, 433
Rachford, B. L., et al. 2002, ApJ, 577, 221
Reach, W. T., Wall, W. F., & Odegard, N. 1998, ApJ, 507, 507
Rice, W., Lonsdale, C. J., Soifer, B. T., Neugebauer, G., Kopan, E. L., Lloyd, L. A., de Jong, T., & Habing, H. J. 1988, ApJS, 68, 91
Rubio, M. 1999, in IAU Symp. 190, New Views of the Magellanic Clouds, ed. Y.-H. Chu et al. (San Francisco: ASP), 67
Rubio, M., Boulanger, F., Rantakyro, F., & Contursi, A. 2004, A&A, 425, L1
Rubio, M., Lequeux, J., & Boulanger, F. 1993, A&A, 271, 9
Schlegel, D. J., Finkbeiner, D. P., & Davis, M. 1998, ApJ, 500, 525
Schmidt, K.-H., & Boller, T. 1993, Astron. Nachr., 314, 361
Schnee, S., Bethell, T., & Goodman, A. 2006, ApJ, 640, L47
Schwering, P. B. W. 1988, Ph.D. thesis, Leiden Univ.
Sembach, K. R., & Savage, B. D. 1996, ApJ, 457, 211
Simon, J. D., Bolatto, A. D., Leroy, A., Blitz, L., & Gates, E. L. 2005, ApJ, 621, 757
Sofia, U. J., Gordon, K. D., Clayton, G. C., Misselt, K., Wolff, M. J., Cox, N. L. J., & Ehrenfreund, P. 2006, ApJ, 636, 753
Solomon, P. M., Rivolo, A. R., Barrett, J., & Yahil, A. 1987, ApJ, 319, 730
Stacey, G. J., Geis, N., Genzel, R., Lugten, J. B., Poglitsch, A., Sternberg, A., & Townes, C. H. 1991, ApJ, 373, 423
Stanimirović, S., Staveley-Smith, L., Dickey, J. M., Sault, R. J., & Snowden, S. L. 1999, MNRAS, 302, 417
Stanimirović, S., Staveley-Smith, L., & Jones, P. A. 2004, ApJ, 604, 176
Stanimirović, S., Staveley-Smith, L., van der Hulst, J. M., Bontekoe, T. R., Kester, D. J. M., & Jones, P. A. 2000, MNRAS, 315, 791
Stepnik, B., et al. 2003, A&A, 398, 551
Strong, A. W., & Mattox, J. R. 1996, A&A, 308, L21
Weingartner, J. C., & Draine, B. T. 2001, ApJ, 548, 296
Wilke, K., Klaas, U., Lemke, D., Mattila, K., Stickel, M., & Haas, M. 2004, A&A, 414, 69
Wilke, K., Stickel, M., Haas, M., Herbstmeier, U., Klaas, U., & Lemke, D. 2003, A&A, 401, 873
Young, J. S., & Scoville, N. Z. 1991, ARA&A, 29, 581